A General Approach for Deriving the Properties of Cirrus and Stratiform Ice Cloud Particles

ANDREW J. HEYMSFIELD, SHARON LEWIS, AARON BANSEMER, JEAN IAQUINTA, AND LARRY M. MILOSHEVICH

National Center for Atmospheric Research, Boulder, Colorado

MASAHIRO KAJIKAWA

Department of Civil and Environmental Engineering, Akita University, Akita, Japan

CYNTHIA TWOHY

College of Oceanic and Atmospheric Sciences, Oregon State University, Corvallis, Oregon

MICHAEL R. POELLOT

Department of Atmospheric Sciences, University of North Dakota, Grand Forks, North Dakota

(Manuscript received 15 September 2000, in final form 14 May 2001)

ABSTRACT

A new approach is described for calculating the mass (m) and terminal velocity (V_t) of ice particles from airborne and balloon-borne imaging probe data as well as its applications for remote sensing and modeling studies. Unlike past studies that derived these parameters from the maximum (projected) dimension (D) and habit alone, the ''two-parameter approach'' uses D and the particle's projected cross-sectional area (A). Expressions were developed that relate the area ratio (A_r; the projected area of an ice particle normalized by the area of a circle with diameter D) to its effective density (ρ_e) and to V_t.

Habit-dependent, power-law relationships between ρ_e and A_r were developed using analytic representations of the geometry of various types of planar and spatial ice crystals. Relationships were also derived from new or reanalyzed data for single ice particles and aggregates observed in clouds and at the ground.

The mass relationships were evaluated by comparing calculations to direct measurements of ice water content (IWC). The calculations were from Particle Measuring Systems (PMS) 2D-C and 2D-P probes of particle size distributions in ice cloud layers on 3 days during an Atmospheric Radiation Measurement (ARM) field campaign in Oklahoma; the direct measurements were from counterflow virtual impactor (CVI) observations in ice cloud layers during the field campaign. Agreement was generally to within 20%, whereas using previous mass–dimension relationship approaches usually produced larger differences. Comparison of ground-based measurements of radar reflectivity with calculations from collocated balloon-borne ice crystal measurements also showed that the new method accurately captured the vertical reflectivity structure. Improvements in the accuracy of the estimates from the earlier mass–dimension relationships were achieved by converting them to the new form. A new, more accurate mass–dimension relationship for spatial, cirrus-type crystals was deduced from the comparison.

The relationship between V_t and A_r was derived from a combination of theory and observations. A new expression accounting for the drag coefficients of large aggregates was developed from observational data. Explicit relationships for calculating V_t as a function of D for aggregates with a variety of component crystals were developed.

1. Introduction

The development of cloud models employing sophisticated schemes for prognosing cloud ice water content (IWC), and the planned deployment of radar in space to map ice cloud properties, have provided a need to accurately characterize the properties of individual and populations of ice particles. In this study, our aim is to characterize the properties of ice particles found in midlatitude and tropical ice clouds, research important to both climate-modeling and remote sensing studies.

Climate-modeling studies require parameterizations of bulk properties—for example, mass-weighted fall speed or extinction coefficient—as a function of a prognosed variable such as the IWC. These variables have been calculated from the measured or parameterized

Corresponding author address: Andrew Heymsfield, 3450 Mitchell Lane, Boulder, CO 80301.
E-mail: heymsl@ncar.ucar.edu

particle size distribution by several researchers, using dimensional relationships of the form $m = \sigma D^{\beta}$, $A = \gamma D^{\kappa}$, and $V_t = aD^b$ to represent the functional dependence, where the coefficients and exponents in the equations depended on habit. For most habits, two or three sets of coefficients were necessary to cover the full range of observed D (Heymsfield 1972; Mitchell 1996, hereafter M96).

Heymsfield and Iaquinta (2000, hereafter HI00) pointed out that there were substantial questions regarding the generality of previous m versus D and V_t versus D relationships. The relationships were subject to error because they were usually derived from different datasets. For example, A might have been taken from in situ data, whereas m had been taken from surface collections. Furthermore, most estimates of m came from observations at the ground, not from within the cloud, where the particle characteristics might have depended upon height relative to cloud top and base, temperature, mode of origin, and a host of other factors.

Given the difficulty in measuring both m and A for individual particles collected within a cirrus cloud, a geometric model was developed (HI00) to derive the three-dimensional structure of bullet rosettes and columns, which are primary cirrus crystal habits. Calculations from the model facilitated the development of a set of m versus D and V_t versus D relationships for rosettes with from one to eight bullets and for columns. The HI00 method was not general, however, in that the aspect ratios (α)—the width/length of bullets and columns—were prescribed from observations for a small number of particles observed by a balloon-borne ice crystal replicator in very cold cirrus. A more general way would have been to use the particle images more directly in some way to prescribe m and V_t.

In this study, we improve upon the HI00 study, by developing a general method for deriving m and V_t for a number of ice particle habits using both D and A. It was logical to use A and D together instead of D alone, as these two parameters are needed to derive several primary ice cloud microphysical and radiative properties: the extinction coefficient and the effective radius, among others. Furthermore, most particle spectrometers (e.g., 2D imaging probes) record both A and D. The technology to measure m from in situ measurements is not yet available; hence, some physically based method for estimating ice particle m is needed.

In the next section, we develop an approach for deriving m from two parameters, D and A, for a wide variety of ice particle shapes. The approach described uses analytic descriptions of ice particle shapes, in situ aircraft measurements, and observations at the ground and in the laboratory. In section 3, we extend this approach to the calculation of V_t, and in section 4 assess the accuracy of the two-parameter approach using in situ and radar data. Section 5 is a summary of the results and a discussion of some of the implications of the study.

2. Development of area ratio–effective density relationships

One measure that was used to quantify how much ice is contained in an ice particle is its effective density ρ_e. The ρ_e is defined as the mass divided by the volume of a circumscribed sphere. Another measure of how much ice is contained in an ice particle is the area ratio, which is A projected onto a horizontal plane, such as a photodiode array of an imaging probe, compared to the area of a circumscribed circle. Most imaging probes on aircraft have been oriented such that they measure A directly. Our goal was to examine whether increasing A_r coincided with increased ρ_e. In this section, we examine the relationship between A_r and ρ_e for a variety of ice particle types. In the first subsection, we present the results for simplified ice particle shapes; in the second subsection, the results from an analytical model; and in the third subsection, the results from laboratory and field observations.

The emphasis in this study was on the types of crystals found in cirrus clouds, including anvils. In midlatitude anvils formed by strong convection and even in deep, synoptically generated cirrus, aggregates dominate the large end of the size spectrum (Kajikawa and Heymsfield 1989). Tropical-anvil ice particle data that we amassed in the Tropical Rainfall Measuring Mission (TRMM) field programs from February to September 1999 have indicated that planar crystals (plates, stellars, and the like) and aggregates (of planar crystals and a variety of cirruslike crystals) are prevalent in anvils. Because planar crystals usually grow at temperatures primarily between $-10°$ and $-20°$C, they must be transported to the upper troposphere in updrafts or regions of strong mesoscale vertical motions and then carried into the anvils. Hence, planar crystals and aggregates were also considered. In the following discussion, the Magono and Lee (1966) habit classification scheme was used. The symbols and acronyms are defined in appendix A.

a. Results for idealized particle shapes

Following are the results of calculations of ρ_e versus A_r relationships for three simple particle types: hexagonal columns (types C1e and C1f, solid and hollow columns, respectively); crossed columns (type C2b), representing a cluster of attached columns (simplified bullet rosettes); and planar crystals (types P1a to P1e and the like).

With reference to Fig. 1, the A_r for columns (which for sizes above 50 μm generally fall with their long axis normal to their fall direction) is

$$A_{rC} = \frac{lw}{\pi/4(w^2 + l^2)} = \frac{4}{\pi}\left(\frac{\alpha_C}{1 + \alpha_C^2}\right), \qquad (1)$$

where α_C is the aspect ratio for columns. The A_r for columns depends uniquely on the aspect ratio, and for

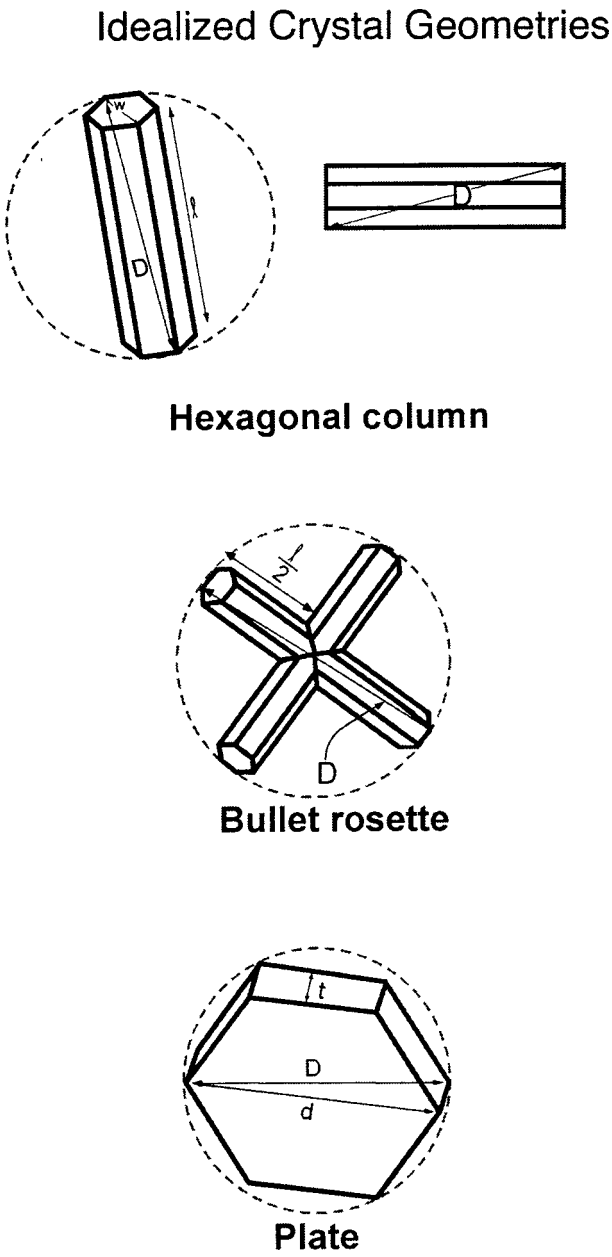

FIG. 1. Geometry and dimensions of three particle shapes: hexagonal columns, bullet rosettes, and plates (P1a).

typical α_C of 0.25–1, A_r ranged from 0.33 to 0.64, the latter being the A_r for $\alpha_C = 1$. For $\alpha_C > 1$, the particle may have been a thick plate (type C1h), falling with the hexagonal face horizontal. In Fig. 1, the maximum projected dimension of the column is D, but most researchers have used l instead of D to represent the maximum dimension.

For this discussion, a rosette is considered to consist of four coplanar hexagonal columns, each column having a length 1/2 and width w. The assumption that the column elements are in the same plane means that none of the column elements overlapped any other element and the length of each element was the same as the projected length. The A_r was

$$A_{rB} = \frac{4\left(\frac{lw}{2}\right) - w^2}{\pi/4(w^2 + l^2)} = \frac{4}{\pi}\left[\frac{\alpha_B(4 - \alpha_B)}{4 + \alpha_B^2}\right], \quad (2)$$

where $\alpha_B = w/(l/2)$. For $\alpha_B = 1$, A_{rB} reached 0.76.

A planar crystal, whose dimension across its basal face was d, had an A_r given by

$$A_{rP} = \frac{A}{(\pi/4)d^2}. \quad (3)$$

The A_r for a hexagonal plate was 0.83. The aspect ratio was given by $\alpha_P = t/d$, where t was thickness.

The ρ_e for a simple column was found to be

$$\rho_{eC} = \frac{\frac{2.6w^2 l\rho_b}{4}}{\pi/6(w^2 + l^2)^{1.5}} = \frac{1.24\alpha_C^2\rho_b}{(1 + \alpha_C^2)^{1.5}}, \quad (4)$$

where ρ_b, the bulk density (m divided by crystal volume), was either 0.91 g cm^{-3} for solid columns or some lower value for hollow columns. The ratio 2.6/4 in Eq. (4) for a hexagon is slightly lower than the ratio $\pi/4$ for a circle. Equation (1) was used to simplify Eq. (4):

$$\rho_e C = 0.764\rho_b(1 + \alpha_C^2)^{0.5}A_r^2. \quad (5)$$

The α_C in parenthesis in Eq. (5) can be solved explicitly[1] in terms of A_r. For comparison with later results, Eq. (5) can be expressed as a power law:

$$\rho_e C = 0.966\rho_b A_r^{2.10}. \quad (6)$$

The ρ_e for a simplified rosette was

$$\rho_{eB} = \frac{\frac{2.6w^2\rho_b(2l - w)}{4}}{\pi/6(w^2 + l^2)^{1.5}} = \frac{1.24\alpha_B^2\rho_b(4 - \alpha_B)}{(4 + \alpha_B^2)^{1.5}}, \quad (7)$$

which, analogous to Eq. (6), was

$$\rho_{eB} = 0.764\rho_b\frac{(4 + \alpha_B^2)^{0.5}}{(4 - \alpha_B)}A_r^2 = 0.510\rho_b A_r^{2.12}. \quad (8)$$

For a planar crystal,

$$\rho_{eP} = \frac{\frac{2.6D^2t\rho_b A_r}{4}}{\pi/6(d^2 + t^2)^{1.5}} = \frac{1.24\alpha_P A_r\rho_b}{(1 + \alpha_P^2)^{1.5}}. \quad (9)$$

The ρ_e for the three simplified shapes are shown as a function of A_r in Fig. 2a, as derived using Eq. (5) with and without the power-law simplification. As an approximation, ρ_b was taken to be 0.81 g cm^{-3} for columns and bullet rosettes and 0.91 g cm^{-3} for hexagonal plates,

[1] Equation (1) was rearranged to yield a quadratic equation, with α_C as the dependent variable. The quadratic formula was used to solve for α_C and yielded $\alpha_C = [2/(\pi A_r)] - [(2\pi A_r)^2 - 1]^{0.5}$.

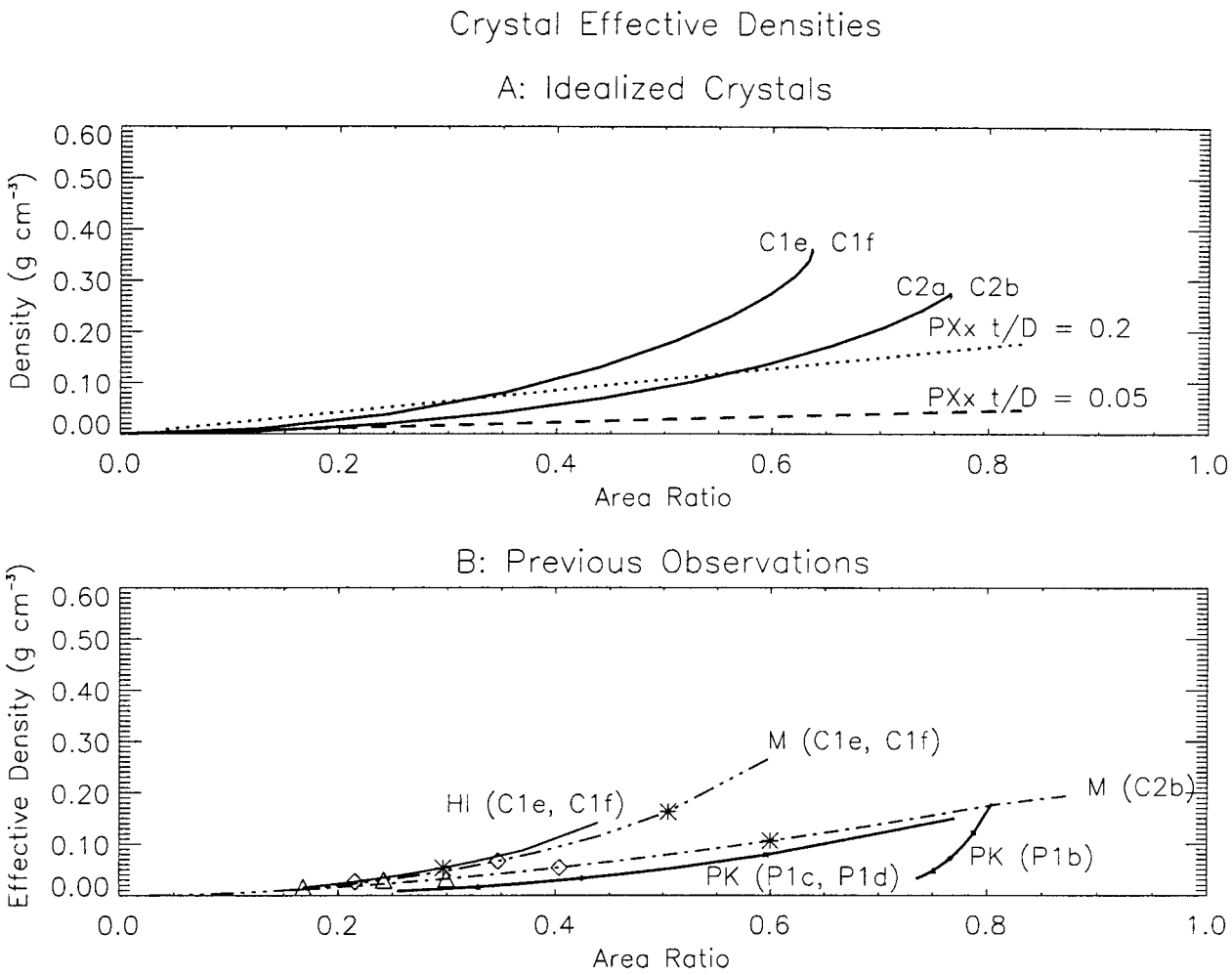

FIG. 2. Calculated ρ_e vs A_r for columns C1e and C1f, simplified rosettes C1b, and plates—PXx (generic), P1c, P1d, and P1e. (a) Simplified particles. Two α_P were assumed. (b) Observations from M96 (M), HI00 (HI), and Pruppacher and Klett (1978) (PK). Symbols along the curves represent three different sizes: 200, 500, and 1000 μm.

based on Heymsfield (1972), HI00, and others. For planar crystals, α_P was taken to be 0.2 and 0.05, representative values from Auer and Veal (1970).

The following conclusions were drawn from Eqs. (4)–(9) and Fig. 2a.

- For columns and crossed columns, $\rho_e \approx \propto A_r^{2.1}$.
- For planar crystals, typically $\alpha_P < 0.2$, therefore ρ_{eP} was linearly proportional to A_r for a given α_P. The ρ_{eP} were lower than ρ_{eC} and ρ_{eB} and were governed by t; t cannot be readily ascertained from imaging probe data unless the probe is oriented perpendicular to the normal sampling orientation and has high resolution (although d is not measured in that case).

We compared these calculations to observations reported in the literature of columns and bullet rosettes (M96 and HI00). Relationships between m and D and between A and D were observed from which ρ_e and A_r were derived. However, these comparisons were approximations because D in these studies differed somewhat from how we defined it for this paper. The resulting relationships between ρ_e and A_r depended on D; these are plotted in Fig. 2b. Points along each of the curves in the figure correspond to D of 200, 500, and 1000 μm; increasing ρ_e along each curve corresponds to decreasing particle size. The general shape of these curves compared favorably with the calculations. Mitchell's ρ_e curve for columns has a shallower slope than the calculations. The M96 curve for five bullets compared favorably with the crossed-column model at the lower A_r values (larger sizes) but fell below the model at the higher A_r values (smaller sizes). Although the curves may have provided reasonable estimates of ρ_e within the range of A_r typically observed, fixed relationships between α and D were required, and the approach may not have produced ρ_e versus A_r relationships that were general.

Plots of ρ_{eP} as a function of A_r based on aspect ratio expressions in Pruppacher and Klett (1978) for types P1b (crystal with sector like branches), P1c (broad

branches), and P1d (stellars) are also presented in Fig. 2b. Points along the curves represent particle sizes. The ρ_{eP} decreased with increasing D, which comparison with Fig. 2a indicates was a result of the decrease in the α_P with D. The A_r for type P1b particles changed only slightly with D, presumably because these crystals did not branch appreciably. Conversely, the ρ_{eP} for type P1c and P1d particles dropped more steeply with A_r than the planar crystals, shown in Fig. 2a, indicates that the α_P decreased with size. The combination of the two planar crystal curves in Fig. 2b suggests that there may be a general relationship between A_r and ρ_{eP} if A_r and α_P are related in some way.

The most important conclusion to be drawn from Fig. 2b is that the m versus D relationships reported previously may not be sufficiently general, because we do not know whether what is being looked at is a dependence of ρ_e on D or a relationship between ρ_e and A_r.

b. *Modeling results for rosettes*

Increasing evidence from observations with new instruments that provide high-resolution images of ice particles suggests that that bullet rosettes (type C2a, combination of bullets) and single bullets are a primary ice particle habit in synoptically generated cirrus clouds (HI00; Paul Lawson 2000, personal communication). Given their significance, and because their 3D geometry has been studied and estimated (e.g., HI00), it is both possible and important to study how their ρ_e and A_r are related.

Bullet rosettes have been found with from one to more than eight component bullets, and the bullets were oriented in a number of 3D configurations. Based on the observations of Kobayashi et al. (1976) and others, Iaquinta et al. (1995) developed an analytic model that represents the 3D rosette geometry. In this model, each bullet was seen to have 10 surfaces: six for the hexagonal body (three rectangles and three pentagons), and four for the pyramidal end (one hexagon and three pentagons). Rosettes containing from one to eight bullets, each bullet with the same dimensions, were described by one of 19 configurations. Rosettes are 3D particles and will have a larger ρ_e for the same A_r and D than the simplified 2D rosettes in Fig. 1 because the bullets are longer for 3D rosettes (see appendix B).

The analytic model described in HI00 was used here to examine the ρ_e versus A_r relationships for 3D rosettes, again in 19 configurations, with from one to eight bullets. A configuration was identified by a given number of bullets, n_b, and a 3D spatial arrangement of the bullets. For each configuration, α_B—ranging from 0.1 to 1, and for a wide range of sizes, were specified; the volume occupied by the bullets in each rosette was then derived. The rosette images were numerically rotated in 3D until the maximum A and associated D were found from the projections onto a horizontal plane. The corresponding A_r and ρ_e[2] (found using the projected dimension D rather than the maximum rosette D) were derived. The ρ_e were related to the A_r, as shown in Fig. 3a, assuming that $\rho_b = 0.81$ g m^{-3} (based on HI00). The curves for all 19 configurations were plotted in the figure to show the range of scatter for all configurations. In general, ρ_e increased with A_r.

The modeling results were simplified to obtain ρ_e versus A_r relationships as a function of n_b. With appropriate averaging, curves of the form

$$\rho_e = k(A_r)^n \tag{10}$$

were derived. The results are plotted in Fig. 3b, and coefficients k and exponents n for n_b from one to eight are shown in Table 1. For a given A_r, increased n_b resulted in lower ρ_e. The explanation for this effect is simple: as n_b increased, the α_B—and hence the bullet and rosette volume and ρ_e—decreased to maintain the same A_r. Also implied from the figure is that increasing n_b produced larger A_r for a fixed α_B. The value of k ranged from 0.47 to 0.66, and a weak, inverse dependence may be seen between k and n_b. The exponent increased from 1.94 to 2.52, and there was a direct relationship between n and n_b. An average ρ_e versus A_r curve was derived for rosettes by averaging over all configurations, but this curve did not capture the dependence reliably and is not shown in Table 1. It is suggested that the three-element curve reliably captures the ρ_e versus A_r relationship for from two to four bullets and the six-element curve does so for from five to eight bullets.

Comparison of the 2D, four-element rosette relationship from Eq. (8) ($\rho_e = 0.41A_r^{2.12}$, with $\rho_b = 0.81$ g cm^{-3}) and the 3D, four-element rosette relationship from Table 1 ($\rho_e = 0.47A_r^2$) indicates that both the k and n for the 2D rosettes are smaller than for the 3D rosettes. This is not surprising because the lengths of 3D bullets are longer than lengths of 2D bullets, even though their projected lengths are the same; thus the ρ_e for 3D bullets is larger for the same A_r.

Photographs of rosettes in the literature (Heymsfield 1972) gave us the impression that $\rho_b < 0.81$ g cm^{-3}, because the hollow ends of the bullets cover a large portion of the projected area. This question was further investigated by examining images of rosettes collected and photographed at the ground in Siberia at temperatures below -30°C by Klinov (1960). Many of the bullets in the rosettes had characteristic hollow ends. For each of 180 bullets, we estimated the hollow volume (v_h) and the bullet volume (v_b) and derived ρ_b from ρ_b(g cm^{-3}) $= 0.91[(v_b - v_h)/v_b]$, as in Heymsfield (1972). Not all of the hollows appeared to be symmetrical, nor were they all conically shaped, although most of them did appear to be. The results plotted in Fig. 3c suggest

[2] Hereafter, subscripts denoting the type of particle associated with a ρ_e − (e.g., ρ_{eB}) are eliminated to reduce overly long subscripts and because it is clear which habits are being referred to.

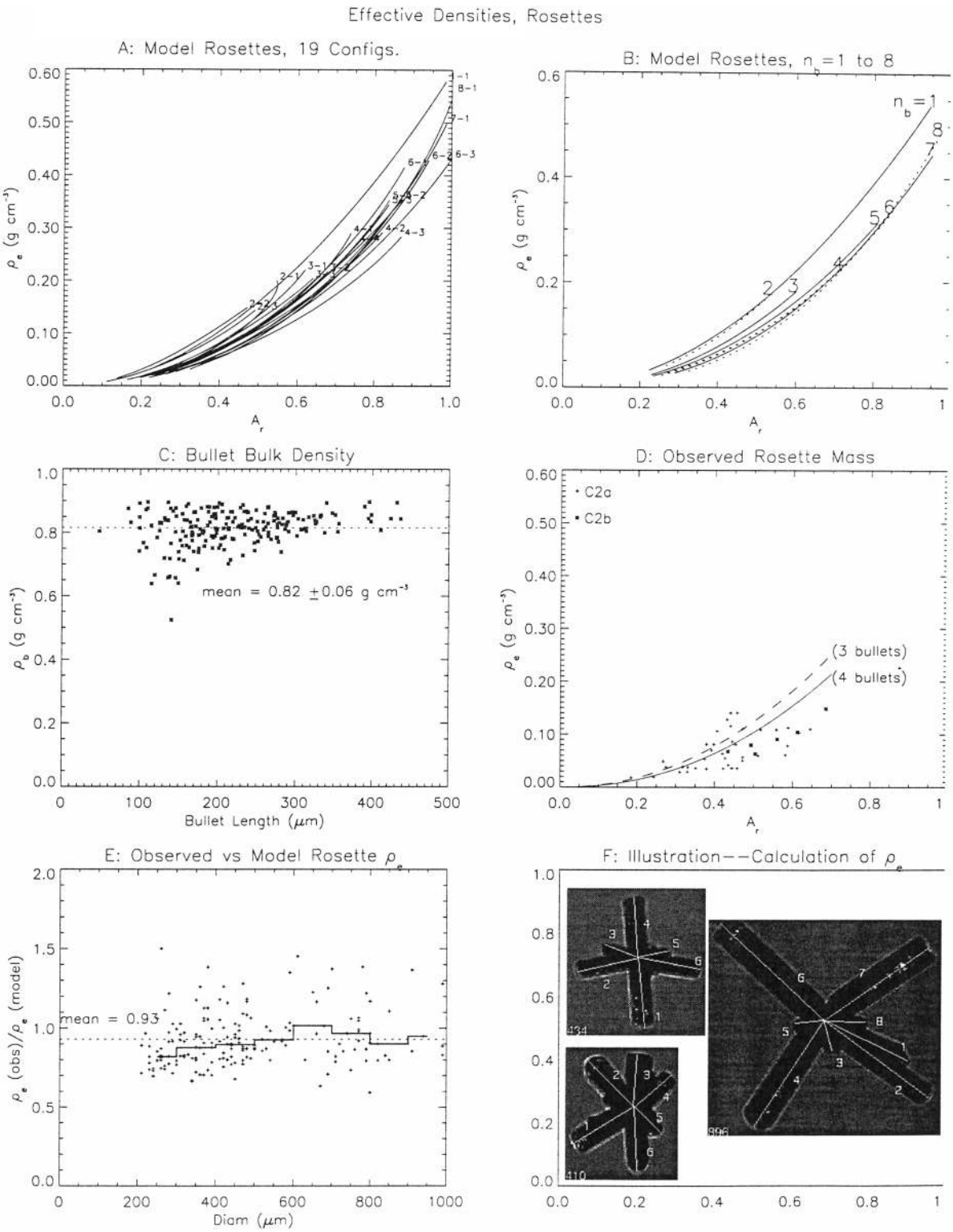

FIG. 3. Calculated and observed ρ_e vs A_r for bullet rosettes. (a) Rosettes, from the 3D analytic model for 19 geometric configurations. (b) Calculations from the 3D model, averaged according to number of bullets. (c) Estimated ρ_b, based on data in Klinov (1960). (d) Measurements by M. Kajikawa at Mt. Hachimantai Observatory of Akita University, Japan, 1200 m MSL. Curves for three—and four—bullet rosettes are plotted. (e) Ratio of ρ_e as calculated from rosettes imaged by CPI on 9 Mar 2000 to ρ_e from analytic model vs D. (f) Examples of rosettes used to calculate ρ_e vs A_r.

TABLE 1. Effective density relations.

Habit	Two-parameter coefficients habit code	$\rho_e = k(A_r)^n$ k	n	r^2	A_r	Range
Columns (theory)	C1e-C1f	$0.97\rho_b$	2.10	1.00	0.05	0.64
Rosettes (theory)	C2a					
No. of bullets		($\rho_b = 0.81$ g cm^{-3})				
1		0.60	1.94	0.99	0.22	0.98
2		0.66	2.11	0.99	0.11	0.55
3		0.54	2.11	0.99	0.16	0.68
4		0.47	2.16	0.99	0.20	0.87
5		0.49	2.16	0.99	0.22	0.87
6		0.49	2.25	0.99	0.26	0.99
7		0.50	2.35	1.00	0.29	0.99
8		0.52	2.52	0.99	0.32	1.00
Side planes, S1–S3, (Observatory)		0.35	2.34	0.79	0.18	0.88
Planar crystals						
Wind tunnel	P1a-P1b-P1d	0.084	2.38	0.97		<0.79
(Takahashi et al. 1991)		11.96	22.64	0.48		≥0.79
Sfc. observations (Heymsfield and Kajikawa 1987)	Many types	0.102	3.29	0.86		<0.81
$A_r = 0.83$	Thick plates	$\rho_e = 0.043$ d$^{-0.529}$				
Aggregates						
Magono and Nakamura (1965)	Planar crystals	0.010	1.50		0.28	1.0
Kajikawa (1982)	2–6 planar crystals	0.015	1.50		0.13	0.77
Agg. side planes (Sfc.)	S1–S3	0.18	1.52	0.97	0.21	0.65
CPI observations (ARM)	Rosettes	0.16	1.48	0.99	0.16	0.56

Aggregate ρ_e vs D relationships
$\rho_e = \chi D^{\delta}$

Aggregate study	Component crystals	χ	κ
Magono and Nakamura (1965)	Planar crystals	0.0142	−1.43
Kajikawa (1982)	2–6 planar crystals	0.00089	−1.23
Side planes (Obs.)	S1–S3	0.0061	−0.92
CPI rosettes	C2a	0.0035	−0.96

Aggregate hybrid approach
$\rho_e = kA_r^n D^{\alpha}$

k	n	α
0.015	1.5	−1.0

that the mean ρ_b was approximately 0.82 ± 0.06 g cm^{-3}. Much of the variance was attributable to measurement uncertainties at the small sizes, although no appreciable dependence on particle size was noted. The magnitudes of ρ_b found in this analysis were comparable to those found by Heymsfield (1972).

c. Observations

1) CIRRUS CRYSTAL TYPES

A dataset containing m, A, D, and V_t for rosettes was recently collected by M. Kajikawa at Mt. Hachimantai Observatory of Akita University, 1200 m mean sea level (MSL), where the surface temperatures ranged from −9° to −11°C. Of the 45 particles observed, 39 were classified as type C2a (combination of bullets) and the remaining as type C2b (combination of columns). Of the 45, approximately 25% of rosettes had $n_b = 2$; 25% had $n_b = 4$; 40% had $n_b = 3$; and 10% had $n_b = 5$. Crystal sizes ranged from 0.038 to 0.161 cm. The A and D parameters were obtained from crystal photographs (Fig. 4), and m from the diameters of the drops resulting from melting the particles in oil. Some of the rosettes were modified during their fall to the ground, as the bullets of a few rosettes had end plates, indicating some growth in the −12° to −18°C temperature range. Nevertheless, the dataset was useful for comparison with the rosette modeling results.

The A_r values for these rosettes are plotted as a function of ρ_e in Fig. 3D, with curves for $n_b = 3$ and $n_b = 4$ from the analytical modeling results plotted in the figure for comparison. A curve fitted to the Kajikawa observatory bullet rosette data was obtained and is plotted in Fig. 3d. The k for this curve (0.46) was the same as that found for four-element rosettes (0.47), but the n was larger (2.33 vs 2.16). The ρ_e fell slightly below the 3D model results, but the observations supported a ρ_e vs A_r dependence.

Information on the ρ_e vs A_r relationship for rosettes

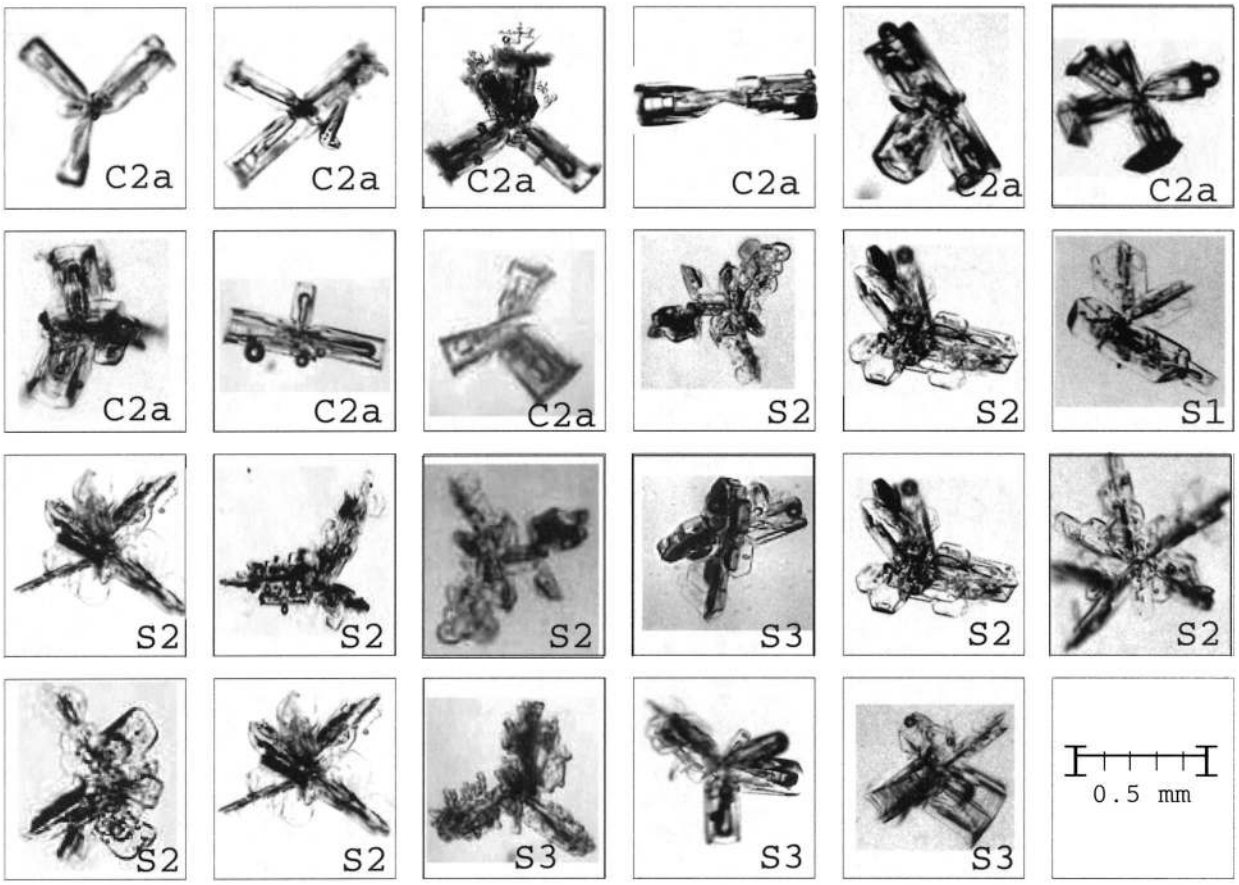

FIG. 4. Examples of rosettes and side planes collected by M. Kajikawa at Mt. Hachimantai Observatory of Akita University, Japan

was obtained using imagery from a SPEC, Inc. cloud particle imager (CPI); images from this probe have resolution of approximately 2.3 μm. The CPI was mounted on the University of North Dakota *Citation* aircraft while participating in an intensive operation program (IOP) near the atmospheric radiation measurement (ARM) site in Oklahoma during March 2000. The particular CPI probe used during the IOP was owned and operated by the National Center for Atmospheric Research (NCAR). A dynamically active band of cirrus, with embedded generating cells and trails (cirrus uncinus), moved over the operations area on 9 March 2000, producing almost exclusively single rosettes and aggregates of rosettes suitable for study. Temperatures at the cloud tops were approximately $-50°$ and $-30°$C, respectively. The rosettes observed on this day had A_r values similar to those observed on other days during the IOP.

We compared the ρ_e values as estimated from the CPI images to those from the analytic model. Referring to Fig. 3f, the volume of ice in each bullet of a rosette was calculated from the w and l, which were measured from the digital images using the National Institutes of Health's image analysis software package. The ice volume of each rosette was then derived by adding together the ice volumes of all bullets in the rosette. The ρ_e values were derived assuming $\rho_b = 0.81$ g cm^{-3}. Here A_r and D measurements were also taken from the images. We examined a total of 180 rosettes, with n_b ranging from one to eight.

These observed ρ_e amounts were compared to the ρ_e values for the same A_r and n_b as obtained from the model. The ratio of the observed to modeled ρ_e as a function of D is shown in Fig. 3e; plots of this ratio against other variables, such as A_r, were not as informative and are not shown. The mean ratio over the measured range of D was slightly below unity, consistent with the modeling results (see appendix B); this shows that the ρ_e values estimated from 2D projections of rosettes were smaller than the actual ρ_e by 10% to 20% because the measured bullet lengths, which represent projected lengths, are smaller than the actual bullet lengths. For reference, the A_r values for the particles considered in Fig. 3e ranged from 0.2 to 0.5. This comparison also shows that the individual bullets became increasingly asymmetric with increasing values of D (see the large rosette in Fig. 3F). Asymmetry, presumably resulting from enhanced vapor growth from ventilation for the bullets on the underside of the rosette, was not considered in the analytic model.

Information on the A_r and ρ_e of side planes (habit types S1–S3) was obtained from observations; 3D modeling of side-plane geometry was beyond the scope of this study. Collections of side planes—from the Kajikawa study (Fig. 4) and by Knight and Heymsfield during cold outbreaks in Boulder, Colorado, from 1984 to 1986—were used to develop a dataset containing A_r and ρ_e information. The Knight and Heymsfield particles were collected in a cold room, photographed in hexane, then rephotographed following melting. A portion of this dataset was presented in Detwiler et al. (1993). A total of 85 particles (15 type S1, 35 type S2, 35 type S3), which ranged in size from 0.038 to 0.168 cm, composed the dataset.

Side-plane ρ_e generally increased with A_r; the resulting curve fit through the data is plotted in Fig. 5a and listed in Table 1. The values for n and k, as well as for ρ_e, fell below those for the 3D model rosettes and the rosette observations. This was not surprising because components of side planes had elongated or linear low-density features; this was especially true for types S1 and S2.

Inspection of Figs. 3 and 5a reveal some general characteristics of rosettes and side-plane-type particles. For a given A_r, rosettes tended to have somewhat larger ρ_e than side planes, on average. Rosette A_r fell in the range 0.3–0.7, with a mean of 0.45 $\pm$ 0.126, whereas side-plane A_r ranged between 0.2 and 0.6, with a mean of 0.39 μm $\pm$ 0.095.

Mitchell's (1996) and Mitchell et al's (1996) relationships between A and D and between m and D for a variety of cirrus crystal types were converted into ρ_e versus A_r relationships for comparison; the results are presented in Figs. 3 and 5a. These studies considered side planes (380–1680 μm) and aggregates of side planes (600–4100 μm), planar polycrystals (20–450 μm), and 5-bullet rosettes (5–1000 μm). The ρ_e values calculated from the various relationships for these particle types are presented in Fig. 5b; A_r amounts ranged between 0.3 and 0.8, and a given A_r corresponded to a given D. The M96 relationships may provide reasonable estimates for ρ_e within the A_r values commonly found for particles of these types.

2) PLANAR CRYSTALS

We should in Eq. (9) that the critical parameter needed to derive ρ_{eP} was the α_P. Wind tunnel observations by Takahashi et al. (1991, hereafter T91) and observations at the ground reported in Heymsfield and Kajikawa (1987, hereafter HK87), were used to examine the ρ_e versus A_r relationships for planar crystals. Takahashi et al. grew several different types of planar crystals, at water saturation and constant temperatures, which were freely supported in a vertical wind tunnel. They measured crystal diameter, area, and mass as a function of time. We are indebted to Prof. T. Takahashi for supplying us with the original wind tunnel observations. We examined the data for four growth temperatures -12.2°C, where hexagonal plates (P1a) evolved to sector plates (P1b) after 7 min; -14.4°C, where broad-branched crystals (P1c) evolved into dendrites (P1e); -16.5°C, where sector plate crystals (P1b) grew; and -18.2°C, where plates evolved into plates with simple extensions (P2e). We also examined the masses and areas of 456 unrimed and rimed planar crystals collected at the ground in Japan (HK87).

We first examined how A_r varied as a function of α_P, with the hope that α_P could be expressed as a function of A_r; if this proved to be so, to establish the physical basis for a ρ_e versus A_r relationship. The α_P values from T91 and HK87 were plotted as a function of A_r (Figs. 6a and b, respectively). The planar crystal thickness was not measured in the HK87 dataset, but an average t was calculated from known parameters: $t = m/[(\pi/4) \cdot 0.91 (A_r D^2)]$. The wind tunnel measurements shown in Fig. 6a indicated that for $A_r < 0.8$, α_P and A_r were related. Curves fitted through the data, plotted in Fig. 6a and listed in Table 2, showed high correlation coefficients for $A_r < 0.80$ but low correlation for $A_r \geq 0.80$. These data suggested, but did not confirm, that a general relationship existed between α_P and A_r, as there was also a direct correspondence between A_r and D (T91).

The HK87 data further supported the idea that there was a general A_r versus α_P relationship (Fig. 6b), with the exceptions of thick plate crystals (type C1h) and hexagonal plates (type P1a) below a hundred or so microns. Both the wind tunnel and observational datasets had similar dependencies (see curve fits plotted in Fig. 6b and listed in Table 2), even though the HK87 dataset included both unrimed and rimed crystals. Type C1h particles did not conform to the observations, and a mean α_P for these particles was derived. Because a rather wide range of particle types and sizes were considered in the HK87 observations, and they conformed to the T91 observations, Eq. (9) suggested that there is a general relationship between ρ_e and A_r for planar crystals with $A_r < 0.80$.

The ρ_e versus A_r data from the wind tunnel and observational datasets are plotted in Figs. 7a and 7b, along with curves fitted to the data for $A_r < 0.80$. The curve fits are listed in Table 1 as planar crystals. Correlation coefficients were nearly unity. In general, the curves fitted to the wind tunnel and observational datasets were comparable.

The two-parameter approach breaks down when $A_{rP} \approx 0.83$, for types P1a (hexagonal plates), P1b (sector plates), and C1h particles. For such situations, a ρ_e versus D relationship was developed (see Table 1, planar crystals, $A_r = 0.83$). Using Eq. (9), this relationship was developed with $A_r = 0.83$ and $\rho_b = 0.91$ g m^{-3}; we also used the Auer and Veal (1970) α_P versus D relationships for crystal types P1a and P1b. A similar relationship has not been derived for C1h particles. In general no means is available for knowing whether a crystal is a thin (P1a) or thick (C1h) plate by viewing

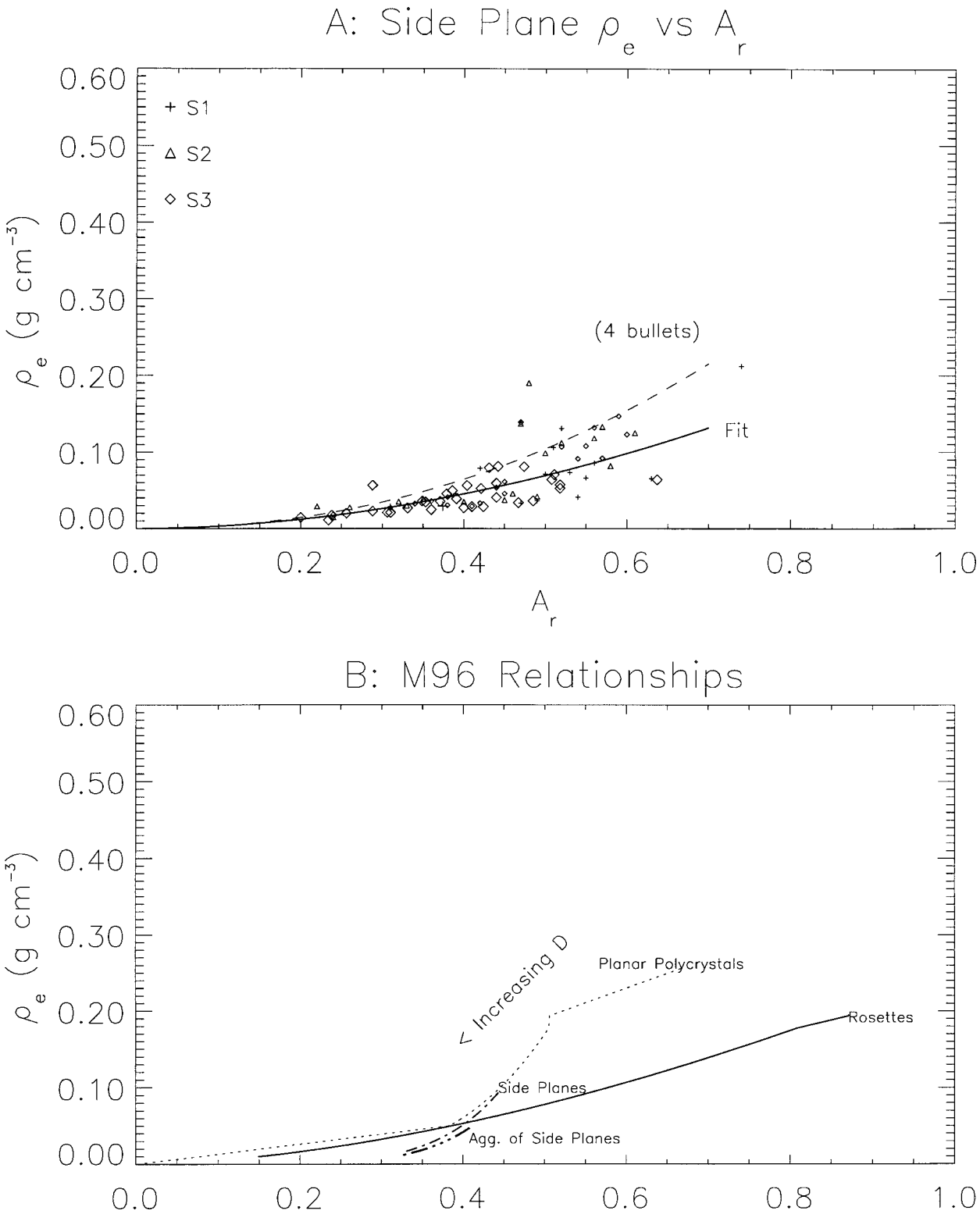

FIG. 5. (a) The ρ_e vs A_r for three types of side planes, based on the data of Kajikawa and the collections at the ground in Boulder, CO, 1700 m MSL. A curve fit to the data is shown, as is the curve for bullet rosettes, $n_b = 4$. (b) Observations from M96 for several different cirrus crystal types.

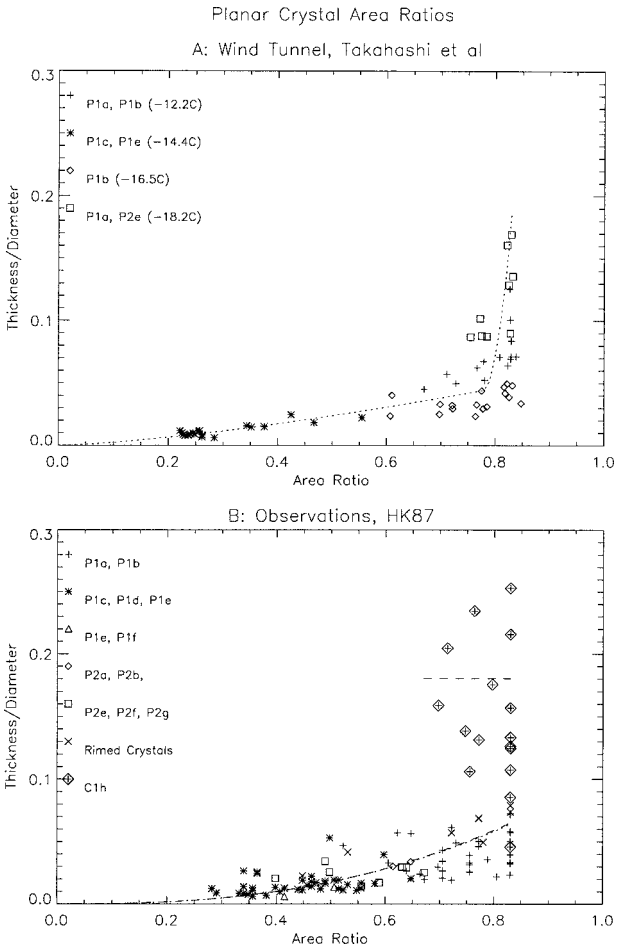

FIG. 6. The α_P as a function of A_r for a variety of planar crystal types for the (a) wind tunnel observations of Takahashi et al. (1991) and from (b) field observations from HK87. Wind tunnel data kindly furnished by T. Takahshai.

from above. However, P1a particles are probably more common, because C1h are usually restricted to very narrow temperatures near −10° and −20°C, and P1a cover a much wider range of sizes.

3) AGGREGATES

Aggregate mass as a function of D was frequently studied in the 1960s through the early 1980s in Japan and in the United States (Magono and Nakamura 1965, hereafter MN65; Locatelli and Hobbs 1974; Sasyo and Matsuo 1980; Kajikawa, 1982). Video distrometers in Switzerland have been used recently to measure aggregate A from the side, A_v (a vertical rather than horizontal cross-sectional area), and V_t (Barthazy et al. 1998). However, the A and corresponding D for aggregates have rarely been studied, so there are virtually no relationships reported between ρ_e, or m, and A along with the corresponding D needed to derive ρ_e versus A_r relationships. In the following discussion, we reanalyze

TABLE 2. Planar crystal aspect ratios.

Source	$v_d = x(A_r)^y$[cgs] x	y	r^2	A_r range
Wind tunnel observations				
	0.0630	1.41	0.91	<0.80
	23.71	26.0	0.41	>0.80
HK87				
No C1h Particles	0.105	2.57	0.75	<0.83
C1h Particles	0.180	0.00	±0.01	<0.83

data from several previous studies to extract both ρ_e and A_r information for aggregates, and we report on our new work, which further studied the problem for aggregates comprising several types of component crystals.

Data from the Kajikawa (1982) and MN65 studies were reanalyzed to obtain A_r and ρ_e information for aggregates comprising planar-type crystals. Kajikawa measured the m and D for aggregates containing from two to six crystals—at the Mt. Teine Observatory of Hokkaido University, at a height of 1025 m MSL. Each

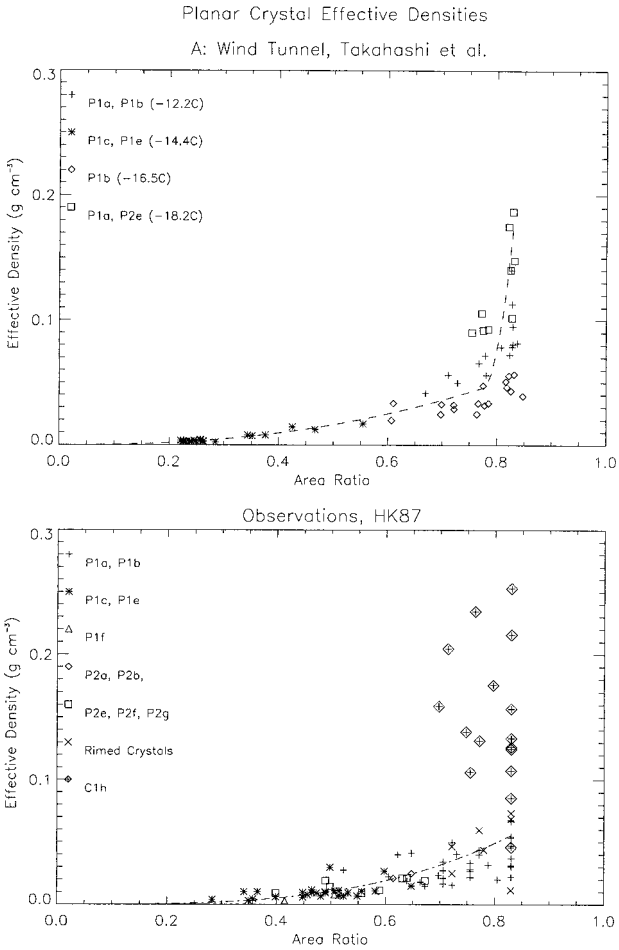

FIG. 7. The ρ_e vs A_r for planar crystals. (a) Wind tunnel observations. (b) HK87 observations.

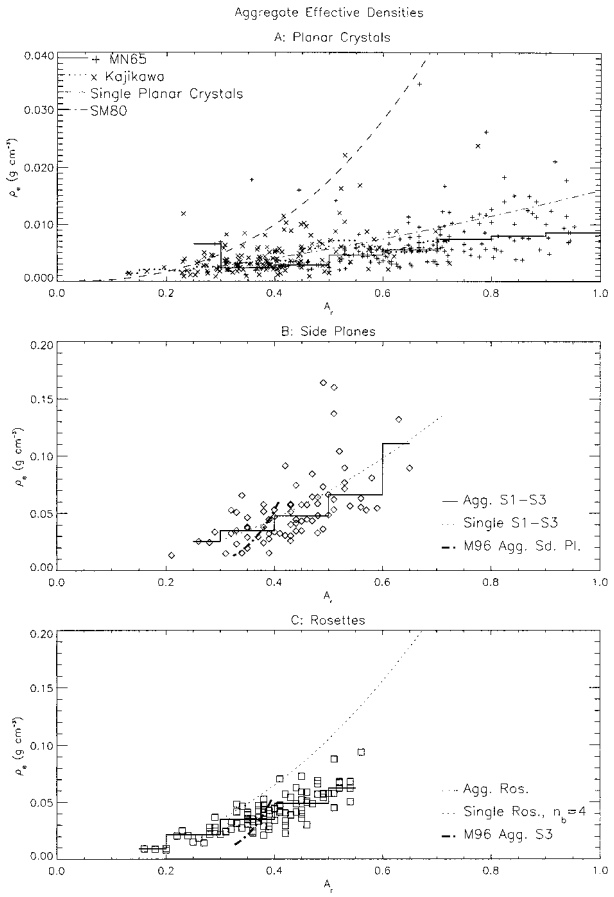

FIG. 8. The ρ_e vs A_r for aggregates with three types of component crystals. (a) Data from MN65 and Kajikawa (1982) for particles that compose primarily planar crystals, with median values of ρ_e plotted in A_r intervals of 0.10 and 0.05, respectively, for each of these datasets. Sasyo and Matsuo (1980) and average curve for individual planar crystals from HK87 are also plotted. MN65 data was kindly furnished by T. Nakamura. (b) Data for aggregates of side planes observed at the ground in Boulder, CO, furnished by N. Knight and one of the authors (A. Heymsfield). Curve for individual side planes based on collections at the ground is shown. The curve deduced from M96 data for aggregates of side planes is shown. (c) Rosettes, based on analysis of CPI data on 9 Mar 2000. Curve for individual rosettes with four bullets is plotted, along with the curve from M96 data for aggregates of type S3 particles.

of these embryonic or ''early'' aggregates was made up of one of the following groups of planar crystals: platelike habits (types P1a–P1c, P2e), branched planar crystals (types P1d–P1e, P2a–P2c), and rimed dendritic crystals (types R1d). From photographs of these aggregates in oil, we derived A and rederived D for 156 aggregates; they ranged from 0.11 to 0.604 cm in size. The resulting ρ_e versus A_r data are plotted in Fig. 8a. For the dataset as a whole, the mean $A_r = 0.40 \pm 0.11$, indicating that the A_r of the early aggregates were generally small. Median ρ_e values in A_r intervals of 0.05 are plotted with dotted lines. Values for ρ_e increased from approximately 0.002 g cm^{-3} at A_r of 0.20–0.006 g cm^{-3} at A_r of 0.60, with considerable scatter. Also plotted in Fig. 8a is a curve for single planar crystals; the ρ_e were considerably larger for the same A_r.

We have been extremely fortunate to have obtained the original data from the MN65 study (kindly furnished by T. Nakamura). In the original notes, the component crystals were referred to as aggregates of ''dendritic crystals,'' ''powdered snow,'' or ''wet snowflakes.'' More than 300 particles composed the dataset, but we eliminated those that may have been partially melted (where the surface temperatures were above 0°C), or that did not have A information. Mass, area, and maximum dimension were recorded for a total of 185 particles, ranging in size from 0.60 to 3.3 cm. Given the difficulty in determining the areas of aggregates with hollow or concave regions, A and A_r were probably overestimated. For the dataset as a whole, the mean A_r was 0.68 ± 0.17, indicating that these particles had relatively high A_r. The median values in A_r intervals of 0.10 were plotted with solid lines (Fig. 8a). The ρ_e increased from approximately 0.003 g cm^{-3} at A_r of 0.30–0.009 g cm^{-3} at A_r of 0.90. Note that MN65 reported on the bulk density of the aggregates (aggregate mass divided by the volume of a circumscribed ellipse). Our reanalysis of the MN65 data indicated that the bulk densities were larger than ρ_e, on average, by a factor of 1.85.

Although considerable scatter was evident in the MN65 and Kajikawa (1982) datasets, both indicated increasing ρ_e associated with increasing A_r. We tried numerous types of fits to the data, separately for each set and also for both sets combined. With little loss of accuracy, we fit each of the datasets to curves of the form $\rho_e \propto A_r^{1.5}$ (Table 1). The exponent 1.5 was chosen so as to be consistent with early observations of aggregates with similar types of component crystals by Sasyo and Matsuo (1980) in Japan. Sasyo and Matsuo found that A_v and m were related by

$$m(g) = 0.012A_v^{1.5}, \tag{11}$$

where the range of m was 0.0001 to 0.01 g; A_v ranged from 0.02 to 1.0 cm^2; and D, although not reported, was estimated to be from 0.1 to 1 cm. Inserting the definitions of ρ_e and A_r into Eq. (11) yielded the equation $\rho_e = 0.016A_r^{1.5}$, which is also listed in Table 1 and plotted in Fig. 8a. Taking A_v to be approximately 0.9A (based on MN65), the proportionality constant in the Sasyo and Matsuo ρ_e versus A_r relationship was, therefore, approximately the same as for the Kajikawa (1982) data (0.015 g m^{-3}) and 60% larger than for the MN65 data.

The ρ_e versus A_r relationship for aggregates comprising side-plane components was obtained from collections in a cold room at NCAR in Boulder, Colorado, by Knight and Heymsfield. The m, D, A, and A_r of 77 aggregates were obtained from the digitized photographs of the particles. The ρ_e values are plotted as a function of A_r in Fig. 8b, with median values of ρ_e plotted in A_r increments of 0.1. In general, ρ_e increased with A_r. A power-law curve fit to the median values is

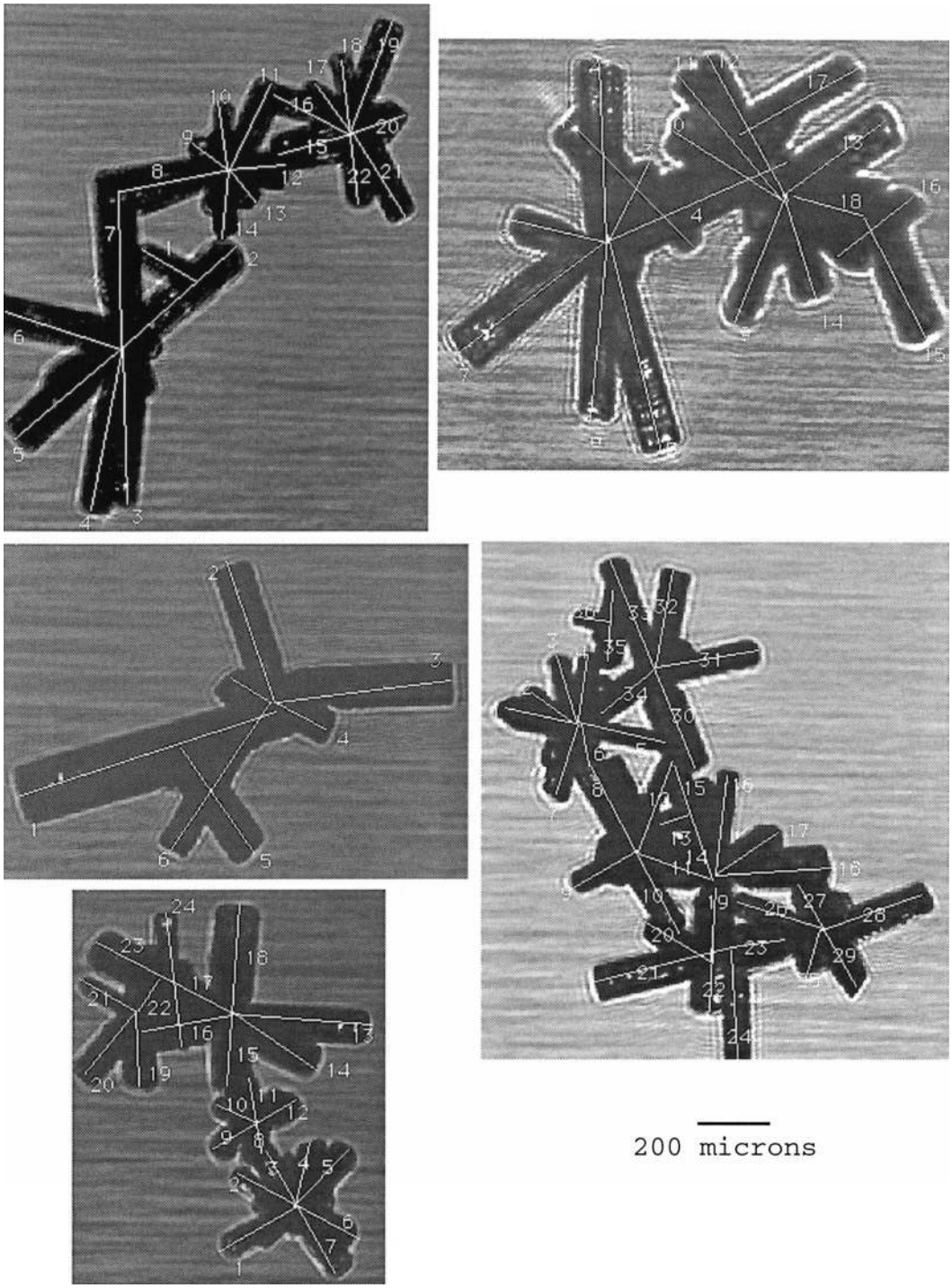

FIG. 9. Aggregates of rosettes imaged with a CPI probe on the University of North Dakota Citation on 9 Mar 2000 in a cirrus cloud, illustrating how *m* for rosette aggregates was derived from the *m* for the individual bullets.

listed in Table 1. These ρ_e values did not differ much from those for individual side planes (curve also plotted in Fig. 8b), but were about an order of magnitude higher than for aggregates of dendrites for the same A_r. The corresponding ρ_e values derived for aggregates of side planes reported in M96 were comparable to those observed here, but the range of A_r was not as large.

Information on ρ_e and A_r for more than 100 aggregates of rosettes was obtained from CPI images on 9 March 2000. The volume of each bullet in each aggregate was

measured, as illustrated in Fig. 9. The ice volume of each aggregate was derived by summing over all bullets in it. This volume was increased upward by 1/0.93, because the projected lengths of bullets in a rosette were on average approximately 93% as large as the true 3D lengths (appendix B). The masses and effective densities for aggregates were obtained by assuming $\rho_b = 0.81$ g cm^{-3}. The A_r for each aggregate was also derived from the image.

A curve fit through the ρ_e versus A_r data for rosette aggregates is plotted in Fig. 8c and listed in Table 1. The ρ_e values for rosette aggregates were equal to or fell slightly below those for single rosettes with $n_b = 4$ over much of the A_r range and were quite close to those for $n_b = 6$ (not shown). The corresponding ρ_e values derived for aggregates of S3 from M96 were comparable to those seen here, but the range of A_r was not as large.

The resulting ρ_e versus A_r relationships for aggregates may be summarized as follows.

- The exponent in the relationship was approximately 1.5.
- The relationships for the cirrus crystal types (side planes, rosettes) were comparable to each other, and the resulting ρ_e values for given A_r increments do not differ appreciably from those for single (unaggregated) particles.
- Values of ρ_e for aggregates of planar crystals are much lower than for the spatial crystal types, ranging from 0.001 to 0.015 g cm^{-3}. The bulk densities of these aggregates are higher than ρ_e, on average by a factor of 1.85, but are still considerably lower than those for aggregates of rosettes or side planes.

The ρ_e for the various types of aggregates can also be examined as a function of D to assess whether there are systematic changes in ρ_e with D that may be inherent in the ρ_e versus A_r relationships. As the symbols in Fig. 10a show, ρ_e generally decreased with D in much the same way as reported in M96 and other studies.

Curves of the form $\rho_e = aD^b$ fitted to the observations are plotted in Fig. 10a over the relevant range of D values and are listed in the middle of Table 1. The slopes of the curves are close to unity, comparable to the slopes deduced from the mass versus diameter relationships for unrimed aggregates of side planes, bullets, and columns by Locatelli and Hobbs (1974) and in M96 of -1.1 and -0.9, respectively.

The observations shown in Fig. 10a suggest to a first approximation for aggregates $\rho_e \propto D^{-1}$, but is modulated by A_r. Drawing upon the general dependence $\rho_e \propto A_r^{1.5}$, we developed a hybrid relationship that embodies the dependence of ρ_e on both A_r and D, $\rho_e = 0.015A_r^{1.5}D^{-1}$ (also listed in Table 1). As shown in Fig. 10b, use of this equation to predict ρ_e reduces the need to have explicit knowledge of the habits of the aggregates. Although this method appears promising, a consistent set of values for mass and A_r over a wide range of habits is needed to establish the generality of the approach and more accurate estimate of the coefficients.

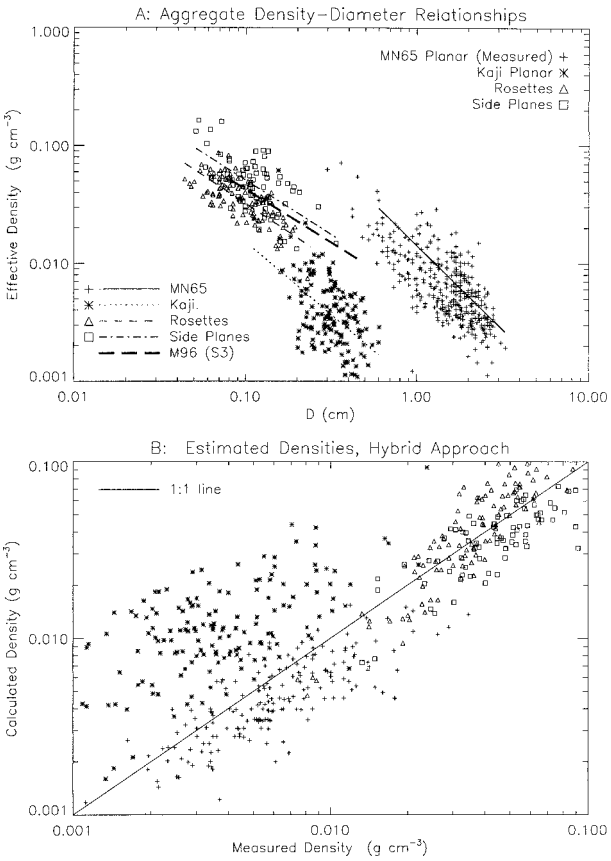

FIG. 10. (a) Aggregate ρ_e vs D for MN65 and Kajikawa (1982) aggregates. Curve fits to the individual habits are plotted and also listed in Table 1. Curve from M96 for aggregates of side-plane type S3 crystals is shown. (b) Measured ρ_e for aggregates from (a) vs those calculated from hybrid equation $\rho_e = 0.015A_r^{1.5}D^{-1}$.

3. Terminal velocity–area ratio relationships

In this section, we describe an approach for deriving terminal velocity using ρ_e and A_r discussed in section 2. The Best number (X) vs Reynolds number (Re) approach, used by a number of researchers, provided a framework for deriving the V_t, which was relatively independent of the ice particle habit. This approach eliminated the need for an explicit drag coefficient; the parameter X was related to the particle drag coefficient C_d through $X = C_d\text{Re}^2$.

The Best number is given by

$$X = \frac{2g}{\rho_a \nu^2} D^2 \left(\frac{m}{A}\right), \tag{12}$$

where g is the gravitational acceleration constant, ρ_a is the air density, and ν is the kinematic viscosity of air. Because

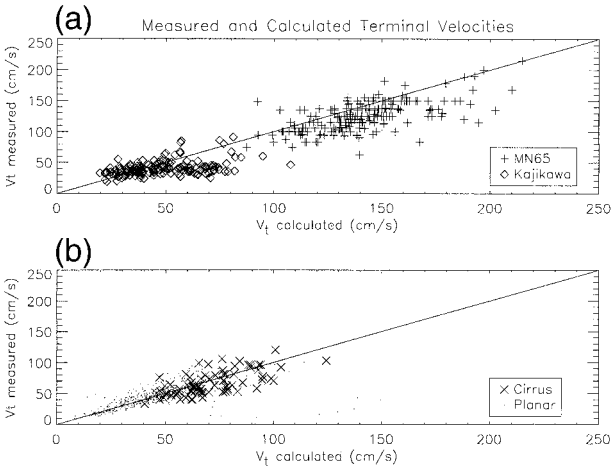

FIG. 11. The V_t calculated using the M96 X vs Re relationships, compared to measurements for (a) aggregates and (b) single particles.

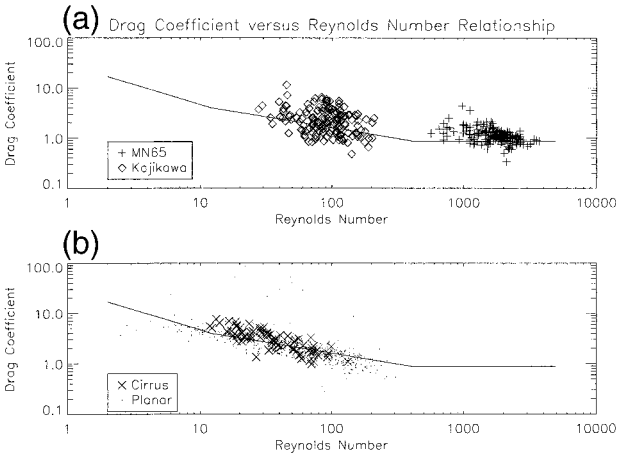

FIG. 12. Drag coefficient vs Reynolds number for (a) aggregates and (b) single particles.

$$\frac{m}{A} = \frac{\pi/6(\rho_e D^3)}{\pi/4(A_r D^2)} = \frac{2}{3}\frac{\rho_e D}{A_r}, \tag{13}$$

Eq. (12) was rewritten as

$$X = \frac{4}{3}\frac{gkA_r^{(n-1)}D^3}{\rho_a \nu^2}. \tag{14}$$

The Reynolds number is given by

$$\mathrm{Re} = \frac{V_t D}{\nu}. \tag{15}$$

A number of researchers have reported relationships between Re and X of the form

$$\mathrm{Re} = a_f X^{b_f}. \tag{16}$$

Solving for V_t in Eqs. (14) and (15),

$$V_t = a_f \left(\frac{4gk}{3\rho_a}\right)^{b_f} \nu^{(1-2b_f)} D^{(3b_f-1)} A_r^{(n-1)b_f}. \tag{17}$$

The following coefficients a_f and b_f were recently reported (M96):

$$\mathrm{Re} = a_f X^{b_f},$$

$$\begin{aligned}
a_f &= 0.04394, \quad b_f = 0.970, \quad 0.01 < X \le 10.0;\\
a_f &= 0.06049, \quad b_f = 0.831, \quad 10.0 < X \le 585;\\
a_f &= 0.2072, \quad b_f = 0.638, \quad 585 < X \le 1.56 \times 10^5;\\
a_f &= 1.0865, \quad b_f = 0.499, \quad X \ge 1.56 \times 10^5.
\end{aligned} \tag{18}$$

Equation (17) provided an explicit means of deriving V_t in terms of D and A_r.

The accuracy of the V_t calculation depends on the accuracy of the coefficients a_f and b_f; values for these coefficients were based primarily on theory and have not been well established from observations, especially for the larger ice particles and for aggregates in particular. Therefore, we have used values for m and A from the various observations at the ground discussed in section 2 to examine the accuracy of the coefficients as given in Eq. (18). The data included in this analysis are from HK87 for planar crystals; the Kajikawa collections for side planes and bullet rosettes; the Kajikawa (1982) observations for aggregates; and the MN65 data for aggregates; they spanned a size range from 0.03 to 3 cm, with Re from 5 to 5000. For each of these particle types, V_t was determined directly from the measurements by combining Eqs. (12) and (15):

$$V_t = a_f \left(\frac{2g}{\rho_a}\right)^{b_f} \nu^{(1-2b_f)} D^{(2b_f-1)} \left(\frac{m}{A}\right)^{b_f}, \tag{19}$$

which is based on the power-law relationships given in Eq. (18). Also, for each particle, X and Re were calculated from Eqs. (14) and (16). The average calculated V_t values were in excellent agreement with those measured V_t for the single (unaggregated) particle types (Fig. 11b), although a few outlying, presumably bad, data points were not omitted from the dataset. For aggregates, however, V_t values were overestimated (Fig. 11a) by 15% on average. This was shown to result from an underestimate of the drag coefficients, plotted in Fig. 12. Each point represents a measurement from the data, and the heavy solid line shows C_d implied from the a_f and b_f coefficients as given in Eq. (18). Note the deviation from the data at $\mathrm{Re} > 700$. Laboratory data from List and Schemenauer (1971) and measurements for graupel from HK87 showed that C_d for $\mathrm{Re} > 700$ tended to increase with increasing Re, possibly because of the onset of tumbling and irregular movements (Kajikawa 1977) or by flow through the particle. The trend was also indicated in the data used for this study.

A correction at these large sizes was found by deriv-

ing a new a_f coefficient and b_f exponent for the largest Re category in Eq. (18):

$$\mathrm{Re} = 1.6353X^{0.465}, \qquad X \geq 1.56 \times 10^5. \quad (20)$$

Unfortunately, very little data are available for values between Re = 200 and Re = 600, so the drag characteristics in this region remain unaccounted for. However, a qualitative comparison of the Re vs X values to those of List and Schemenauer (1971) and in HK87 suggested that the drag coefficients were reasonable.

Several general relationships may be inferred from Eqs. (17) and the coefficients in Eqs. (18) and (20). For synoptically generated cirrus, containing particles of several hundred to one thousand microns, $b_f = 0.831$; therefore, nominally $V_t \propto D^{1.49}$. Most studies have shown that A_r decreases with D (by dividing the M96 A vs D equations by $\pi/4D^2$), therefore the exponent $<$ 1.49. The exponents were recently shown to fall in the range 0.70 to 1.30 for particles of these sizes by Matrosov and Heymsfield (2000).

4. Application

In this section we examine whether the two-parameter approach is both reasonably accurate and useful. The technique was first used to calculate the IWC from 2D imaging probe measurements for three ice clouds, two of which were cirrus; the IWCs in these situations were also measured directly using a counterflow virtual impactor (CVI) (Twohy et al. 1997). Comparison of the calculations and measurements allowed us to assess the accuracy of the technique. The method was applied again when our balloon-borne ice crystal replicator (Miloshevich and Heymsfield 1997) was launched from the operations site during the First ISCCP Research Experiment (FIRE)-II field program in Oklahoma and ascended into a cirrus cloud at the same time that a vertically pointing millimeter cloud radar was measuring radar reflectivity. The replicator measurements in the cloud layer were obtained about 20 km downwind of the radar measurements, but radar observations in this case indicated that the reflectivities were relatively steady in time at given heights (Orr and Kropfli 1999). Therefore, a comparison of the calculated and measured radar reflectivity provided an indirect means of assessing whether the two-parameter approach provided realistic estimates in the vertical.

Two bulk properties of particle size distributions were examined—IWC and equivalent radar reflectivity factor (Z_e or dBZ_e). The basic parameter needed to calculate each of these parameters is m, which was derived from

$$m = \frac{\pi}{6}D^3 \rho_e = \pi D^3 k(A_r)^n, \quad (21)$$

where the coefficients and slopes k and n are those presented in Table 1, and D is the projected dimension.[3]

a. Comparison of IWCs in ice clouds

We were extremely fortunate to have had data from cirrus clouds on 3 days to assess the performance of the two-parameter approach. The measurements were made from the University of North Dakota Citation aircraft. The NCAR–Oregon State University CVI, a probe that directly measures the condensate mass above a threshold size of about 7 μm in diameter, provided an accurate measurement of the IWC (Twohy et al. 1997). The CVI had an IWC detection limit of about 0.003 g m^{-3}, with a 50% uncertainty at that level. The uncertainty decreased to 20% at 0.010 g m^{-3}. High-resolution images of the ice particles from the SPEC, Inc. CPI provided the information necessary to discern habits and the appropriate k and n parameters. Finally, size distributions were measured with PMS 2D-C and 2D-P probes, for the size ranges from 33 to above 1000 μm, and 200–6000 μm, respectively. The software used to analyze the 2D-C and 2D-P data retained the features reported on by Heymsfield and Parrish (1978) but added improvements to find the true D, not the D along the array or time axis.

This improved measure for D also improved the accuracy of A_r, because A_r depends on D as well as A. The 2D-C concentration measurements were used from the minimum detectable size to approximately 1000 μm, and the 2D-P data for 1000 μm and above.[4]

The data for case 1 were acquired on 9 March 2000 during a Lagrangian spiral descent over the Department of Energy–ARM site in Oklahoma in a band of cirrus clouds composing a group of generating cells. Particle habits above about 100 μm consisted almost exclusively of rosettes and aggregates of rosettes (Fig. 13). The mean number of bullets measured from CPI images for 869 rosettes was $n_b = 5.8 \pm 0.6$, within a range $2 \leq n_b \leq 12$. The value $n_b = 6$ was used for the calculations. Although rosette aggregates were observed in the larger sizes, the data, plotted in Fig. 8c, showed that rosette aggregates have approximately the same ρ_e over much of the observed range of A_r as do bullet rosettes with n_b from 4 to 6. Therefore, the k and n for unaggregated rosettes was used for all particles.

[3] For all particle types, D was defined by the maximum size of the projected dimension of a particle. This was the exact dimension used for rosettes by the analytic model, for side planes, for aggregates of these types, for aggregates of dendrites, and for hexagonal columns [$D = (w^2 + l^2)^{0.5}$]. The exception was for planar crystals—$D = d(1 + \alpha_p^2)^{0.5}$—as α_p values were usually small (Fig. 6), $D \approx d$.

[4] A number of studies have shown that the 2D-C probe concentrations are underestimates below approximately 100 μm. We chose not to add additional particles to account for this underestimate because the cirrus clouds studied had a dominance of large particles. We also noted that the 2D-C probe underestimated the A_r below 200 or 300 μm, a feature we have not considered here but we will report on in a future study.

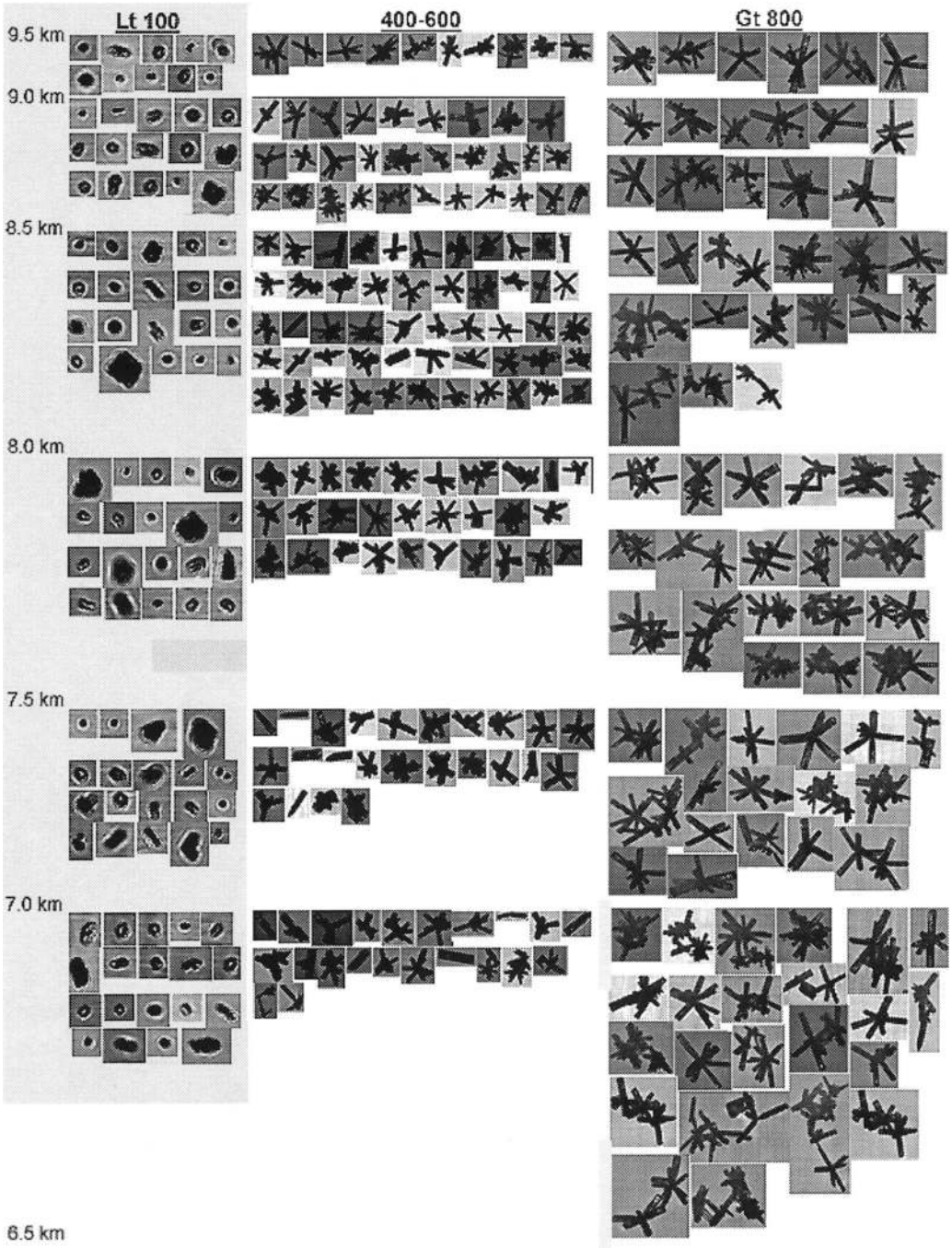

FIG. 13. Example of images collected by CPI probe during Lagrangian spiral descent on 9 Mar 2000, over the ARM site in Oklahoma. Particles are grouped into three size ranges, with different scales.

Time series of measured and calculated IWCs averaged over 5-s intervals during the Lagrangian spiral descent are plotted in Fig. 14. The spiral commenced near −50°C and ended near −26°C (top right panel). Measured IWCs from the CVI (top left panel) increased gradually with time (height below cloud top), and peak IWCs were about 0.1 g m^{-3}. The panels below these show the calculated IWCs from the combined 2D-C and 2D-P data using the following methods: the two-parameter approach, followed by use of various mass versus dimension relationships: the habit-independent equation of Brown and Francis (1995; hereafter BF95), based on Locatelli and Hobbs (1974); five bullet rosettes of M96 and Mitchell et al. (1996); rosettes by Heymsfield (1975), based on direct collections of cirrus particles; and the rosettes by HI00, assuming $n_b = 6$. Coefficients

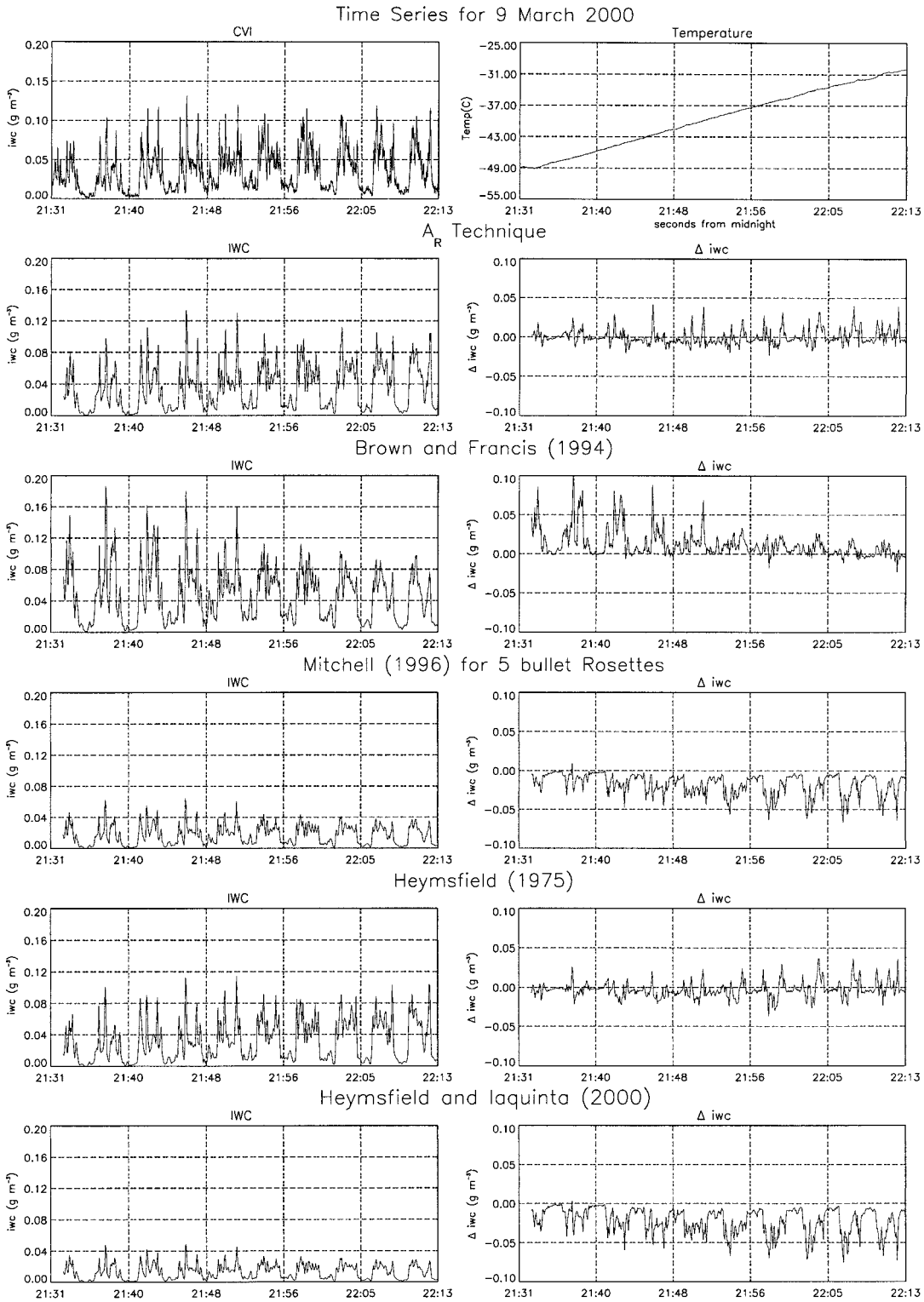

FIG. 14. Time series of 5-s averages of IWC and temperature from the University of North Dakota Citation on 9 Mar 2000 over the ARM site. (top left) Measurements from the CVI. (top right) Temperature. Second through fifth panels are (left) the IWCs and (right) ΔIWCs [IWC (calculated)-IWC (CVI)] as calculated from 2D-C and 2D-P size distributions using the two-parameter approach and the relationships of Brown and Francis (1994), Mitchell (1996), Mitchell et al. (1996), Heymsfield (1975), and Heymsfield and Iaquinta (2000), respectively.

TABLE 3. Rosette mass–diameter ($m = \sigma D^{\beta}$) relationships in previous research.

Researchers	σ (cgs)	β	Size range (cm)
Brown and Francis (1995)	0.476	3.0	$D \leq 0.0106$
	0.00294	1.9	$D > 0.0106$
Heymsfield (1975)	0.476	3.0	$D \leq 0.0026$
	0.00145	2.03	$0.0026 < D \leq 0.003$
	0.044	3.0	$D > 0.03$
Heymsfield and Iaquinta (2000)	$0.000012n_b$	1.52	$D \leq 0.009$
	$0.000399n_b$	2.27	$D > 0.009$
Mitchell et al. (1996)	0.10	2.997	$D \leq 0.01$
	0.00308	2.26	$D > 0.01$

in these mass versus dimension relationships are listed in Table 3.

In the second through sixth panels on the right in Fig. 14, we show the differences between the IWCs as calculated from the size distributions for each technique and those measured by the CVI, (ΔIWC), obtained for 5-s averages of each. For the two-parameter approach, typical ΔIWC values were 0.02 g m^{-3} (20% accuracy) or less, mostly overestimates. The ΔIWC values did not change much with time (altitude), meaning that no biases resulted from particle size, which increased on average downward (see Fig. 13). The ΔIWC values found using the BF95 approach were small in the lower half of the layer but very large and positive in the upper part of the layer, where particles were smaller. Using the HI00 and M96 techniques, we found ΔIWC that were relatively small and negative in the upper third of the spiral where the particles were relatively small, but became increasingly negative with height. The ΔIWCs calculated using the Heymsfield (1975) coefficients compared favorably with the measurements, throughout the layer.

A reliable *m* versus D relationship can be developed to represent the cloud layer by making use of the results from the two-parameter approach for this cirrus cloud.

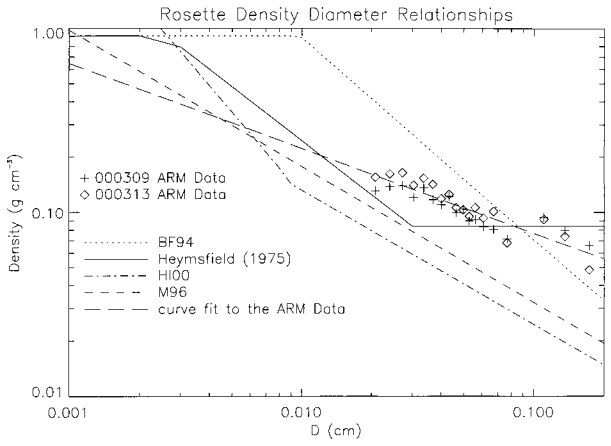

FIG. 15. The ρ_e vs *D* relationships from a number of studies (curves) based on the relationships in Table 3. Superimposed are ρ_e values as a function of *D* as deduced from the two-parameter approach, and a curve fitted to the data.

By taking the amount of IWC in each 2D-C or 2D-P size bin and dividing by the concentration in the bin, an average *m* per size bin was obtained. These *m* per size bin were averaged through the cloud depth. Figure 15 shows the results of this exercise, where the *m* have been divided by $(\pi/6)D^3$ to obtain ρ_e. The mass versus dimension relationships used in Fig. 14 and listed in Table 3 are also converted to ρ_e versus *D* relationships and are plotted in Fig. 15. At the smaller *D*, ρ_e fell below the ρ_e versus D curve obtained using the BF95 coefficients, which is why the BF95 approach overpredicted the IWCs in the upper part of the layer; at the larger *D*, calculations obtained from the BF95 coefficients fit the ''observed'' values reasonably well. The ρ_e versus D curve using the earlier Heymsfield (1975) coefficients fit the observed ρ_e to within a factor of two over a wide range of *D*. The coefficients in the M96 and HI00 relationships yielded values for ρ_e that fit the observed ρ_e reasonably closely when *D* were small but departed by an increasing amount with increasing *D*.

The data for case 2 were acquired over a period of 2.5 h during a step-down and step-up flight pattern near the Oklahoma ARM site on 13 March 2000; temperatures ranged from −50° to −31°C (Fig. 16, top right panel). Again, habits were dominated by rosettes, with n_b values similar to those found on 9 March. The IWCs were derived in 5-s intervals from the 2D-C and 2D-P data, and the *n* and *k* for $n_b = 6$ were used. The peak IWCs were higher than on 9 March, but the mean IWC over the period was lower. Note that this case differed from the 9 March case in that generating cells with large particles were not as prevalent, and smaller particles, some below the 2D-C probe's detection threshold, may have contributed appreciable IWCs.

The results were similar to those found for 9 March. The two-parameter approach produced accurate results throughout the period, except from 2020 to 2050 UTC, where the IWCs were underestimated; we suspect that particles below the detection threshold of the 2D-C probe were contributing a modest amount of IWC to the CVI. The BF95 approach resulted in calculations of low ΔIWCs at the warmer temperatures (larger particles) but yielded relatively large ΔIWCs at the lower temperatures (smaller particles). The M96 and HI00 *m* versus *D* relationships produced accurate estimates at the

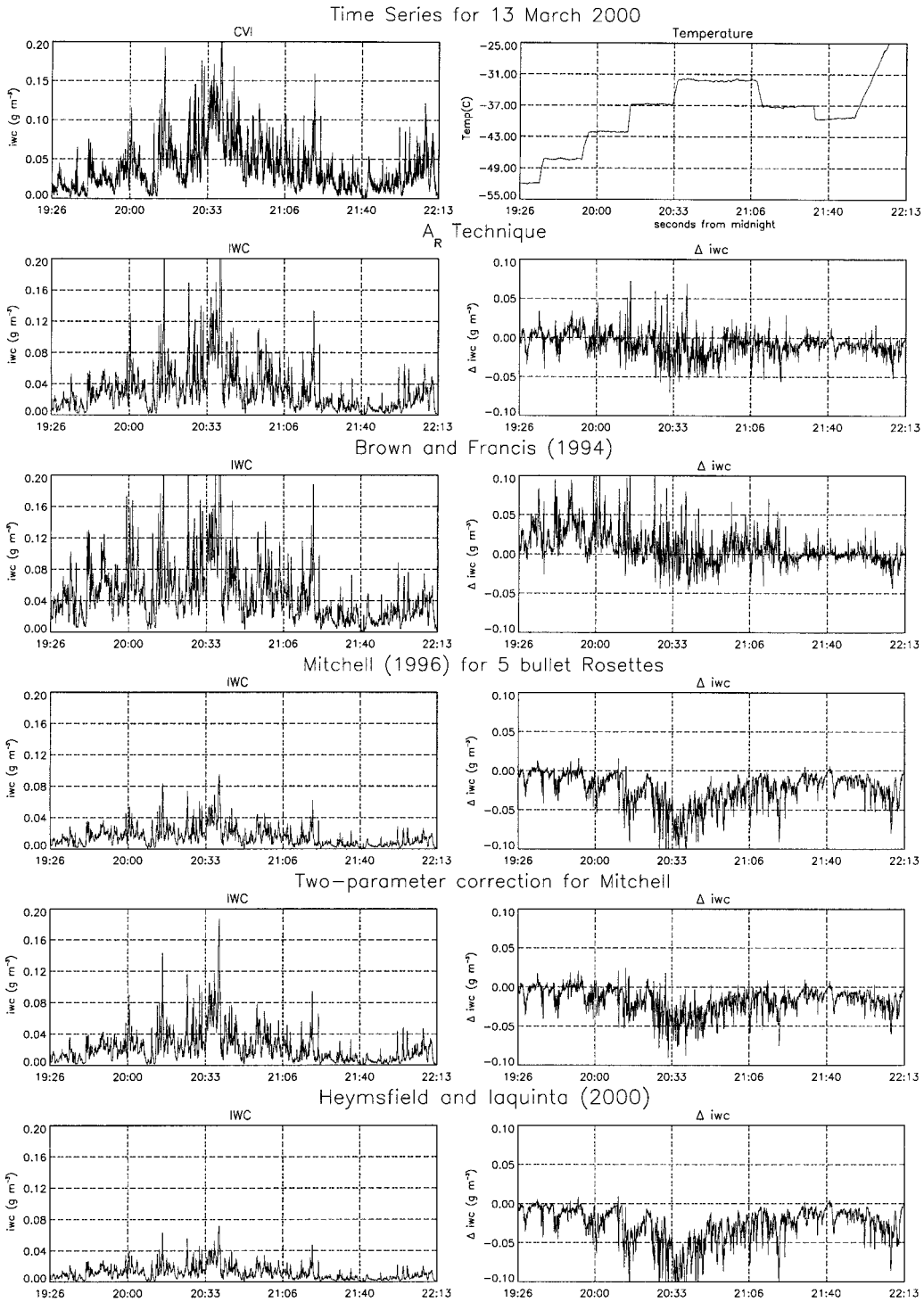

FIG. 16. Time series of 5-s averages of IWC and temperature in cloud layer over the ARM site on 13 Mar 2000. The panels are the same as in Fig. 14, except that the 5-bullet rosette relationship of Mitchell (1996) is converted to a two-parameter approach, and results from the Heymsfield (1975) relationship are not shown.

lower temperatures but gave significantly underestimated IWCs at the warmer temperatures.

To examine whether m versus D relationships posited in earlier studies could be improved if they were adapted to the two-parameter technique, we took the mass and area dimensional relationships for five-bullet rosettes from M96 and combined them to obtain a ρ_e versus A_r relationship (see Fig. 2b). If we compare the bottom two

panels in Fig. 16, we find that use of the two-parameter technique reduced the ΔIWC amounts by about 50% through most of the flight, that is,—substantially improved the IWC estimates.

The ρ_e versus D data from the two-parameter approach for this case was similar to that observed for the 0309 case (Fig. 15). Comparison of these data with the curves in Fig. 15 explains why the BF95 approach overestimated the IWCs at the lower temperatures (small particles) and the HI00 and M96 relationships underestimated the IWCs at the higher temperatures (large particles).

A ρ_e versus D relationship representing the rosettes in the cloud layers sampled on 0309 and 0313 was derived by fitting a curve to the data points in Fig. 15:

$$\rho_e = 0.0265D^{-0.46}\text{cgs}. \quad (22)$$

The m versus D relationship can be found by multiplying ρ_e by $(\pi/6)D^3$.

Case 3, a deep ice cloud layer over the Oklahoma ARM site on 12 March 2000, presented a large proportion of side-plane-type S3 particles and allowed us to evaluate the performance of the two-parameter approach for habit types different than bullet rosettes. The data were acquired over a period of 1–5 h during a stepdown flight pattern, with temperatures ranging from −31° to near 0°C (Fig. 17, top right panel). For $T <$ −15°C, habits were dominated by side planes (primarily type S3) and planar polycrystals. For $T \geq -15$°C, the S3 and planar polycrystal particle habits aggregated and grew branched components. Light crystal riming and liquid water (at most, a few hundredths g m^{-3} measured by the forward scattering spectrometer probe) were occasionally observed. The IWCs were high throughout, at times reaching or exceeding the CVI's saturation limit of approximately 1 g m^{-3} after about 0020 UTC.

As shown by the right panels in Fig. 17, the two-parameter technique using the side-plane coefficients in Table 1 yielded underestimates of the measured IWC (before 0020 UTC) by about 0.10 g m^{-3}, or 20%, with perhaps a slight increase in ΔIWC with time (decreasing altitude) noted. However, the ΔIWC values obtained using the rosette coefficients were closer to the observations, with no systematic trend with time. The BF95 coefficients produced slightly larger negative ΔIWC than for side planes, and even somewhat larger negative ΔIWC were produced using the M96 relationship for side planes (which does not differ much from those for planar polycrystals, which were also observed). As the particles were primarily of type S3, which contain rosette components (see Fig. 4), it is not surprising that the rosette k and n coefficients produce reasonable IWCs.

The deduced ρ_e values as a function of D were examined, and were about 50% larger than the ρ_e values shown for rosettes in Fig. 15.

b. Comparison of reflectivities in ice clouds

On 25 November 1991, during the FIRE-II experiment, the vertically pointing National Oceanic and Atmospheric Administration (NOAA) K_a-band radar located near Coffeyville, Kansas, was probing a cirrus cloud at the same time that our balloon-borne ice crystal replicator penetrated the cloud layer. The radar observations, from 1344 to 1400 UTC, were reported by Orr and Kropfli (1999), and the replicator observations reported in HI00. The more uniform part of the radar-observed cirrus layer extended from 7.5 to 8.5 km. A ragged base and virga—indicating sublimation—extended down to 7 km, and cirrus extended up to 9 km. Shown in Fig. 18 are the individual dbZ_e points as a function of height over the 16-min period; the radar reflectivity pattern during the period was relatively steady, with a variation of only a few dB at a given altitude.

Our balloon-borne ice crystal replicator was launched at 1337 UTC from the same ground site as the radar and ascended at a rate of about 4 m s^{-1}. It passed through the cloud layer between 1408 and 1417 UTC, approximately 20 km downwind of the launch site (as determined from the balloon's latitude–longitude coordinates). Given the wind velocities, this region of cirrus would have been over the ground site from approximately 1345 to 1400 UTC. Replicator-derived cloud-top and cloud-base temperatures were −55° and −30°C, respectively.

The D and A_r were measured for each replicator particle. Size distributions—that is, number concentrations (N) as a function of D—were then derived for 28 layers, each about 100 m deep, from which the dBZ_e values were calculated:

$$Z_e = \sum N(D)D_m^6 = \left(\frac{6}{\pi\rho_w}\right)^2 \sum N(D)m^2, \quad (23)$$

where D_m is the melted equivalent diameter; the equivalent radar reflectivity, which the radar measured, was given by

$$\text{dB}Z_e = 10\log_{10}Z_e - 7.0. \quad (24)$$

The summation in Eq. (23) was carried out over all particles in a given averaging layer. Rosettes dominated in the middle and lower portions of the cloud, and quasi-spherical particles—presumably rosettes in the developing stages (much like the CPI images < 100 μm shown in Fig. 13)—predominated near the top.

The calculated and measured dBZ_e, for $n_b = 2$, a lower bound, and $n_b = 4$ are compared in Fig. 18; each n_b gave about the same dBZ_e and the plotted lines lie on top of each other in the figure. Replicator cloud top extended almost 1 km above the radar-measured top, even though the radar had a minimum detectable reflectivity of about −40 dBZ_e. Within the body of radar-detectable cloud, excellent qualitative and quantitative

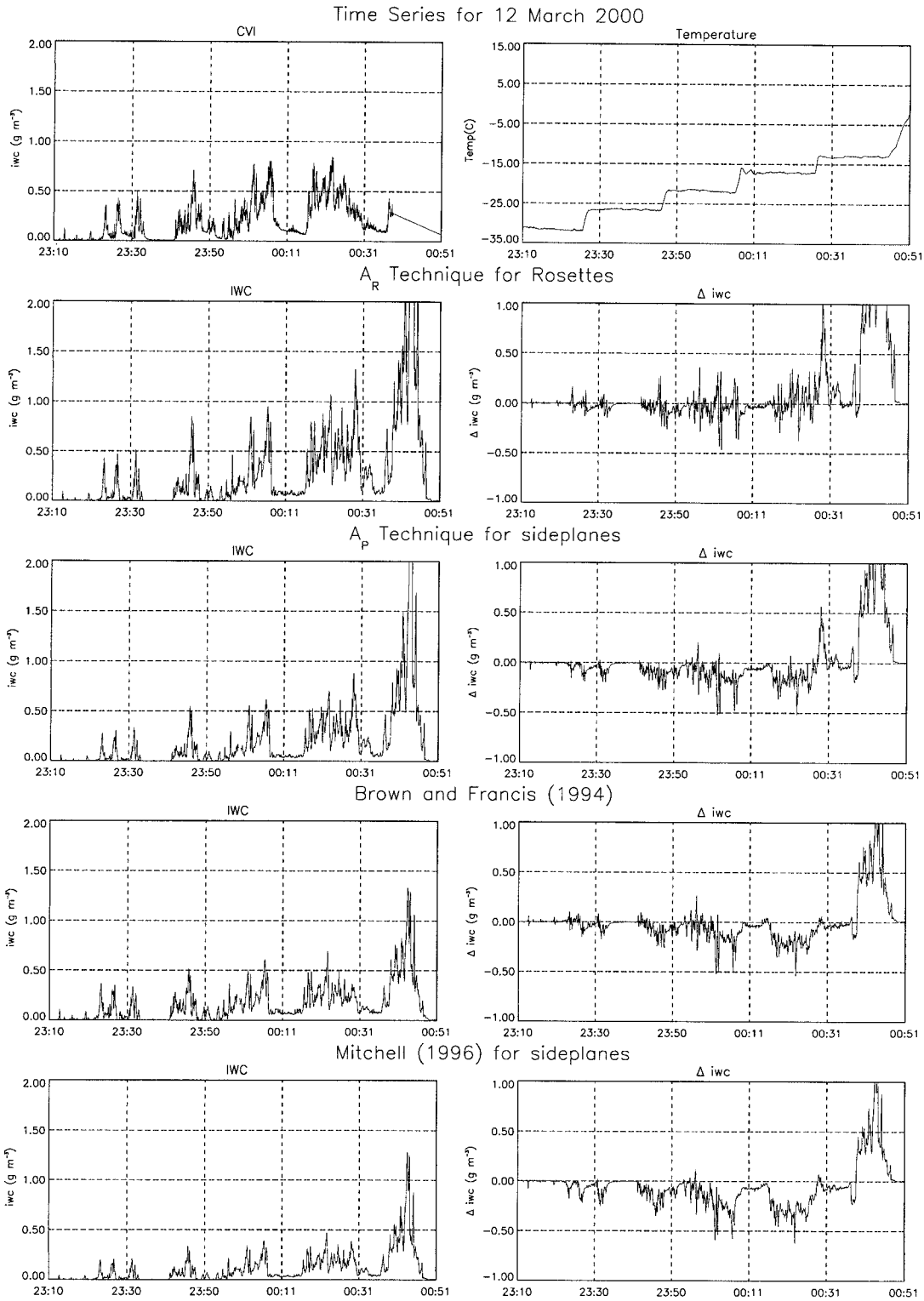

FIG. 17. Time series of 5-s averages of IWC and temperature in cloud layer over the ARM site on 12 Mar 2000. The methods used in the various panels are similar to Fig. 14, but with the habits changed as indicated.

agreement was found between the calculated and measured values.

The dBZ_e as calculated based on previously posited m versus D relationships are plotted in Fig. 19. These various formulations—from M96, HI00, and BF95—did not compare nearly as favorably as the two-parameter approach. This finding paralleled the results for the three ARM cases. In the higher cloud levels, where the particles were relatively small, the M96 and HI00 methods underestimated dBZ_e by about 5 dB; in the BF95 method, dBZ_e values were overestimated by about 5 dB. In the mid to lower cloud levels, where the crystals were relatively large, the M96 and HI00 methods underestimated the dBZ_e, whereas BF95 values were comparable to the measurements. Near cloud base, where the particles were again small, M96 and HI00 approaches provided reasonable results, but the BF95 method yielded overestimates of about 5 dB.

c. Results for aggregates

In this subsection, we examine the accuracy of the ρ_e versus A_r and X versus Re expressions given by Eqs. (17) and (18), and we offer a simplified means of deriving aggregate V_t directly from D.

We first examine how well the two-parameter approach predicts the mass for aggregates of planar crystals. The ρ_e for each of the Kajikawa (1982) aggregates was calculated using $k = 0.01$ and $n = 1.5$ from Table 1 and for the aggregates in the MN65 study $k = 0.015$ and $n = 1.5$ also from Table 1. The calculated and measured ρ_e are compared in Fig. 20a. This comparison is less than ideal as the ρ_e versus A_r relationships were derived from the MN65 and Kajikawa (1982) datasets, but does offer a means of examining how well the relationships fit the data. Although a considerable amount of scatter is evident about the 1:1 line in Fig. 20a—some natural and some resulting from experimental errors—the two-parameter approach produced reasonable estimates of ρ_e for these aggregates. More data (from aircraft measurements using the CVI, 2D, and CPI probes in deep stratiform ice clouds) are obviously needed to refine the estimates of ρ_e for aggregates.

We next examine how well the coefficients in the X versus Re relationships given by Eqs. (18) and (20) predict the terminal velocity of aggregates of planar crystals when m, A_r, and D are known; this comparison is a test of the new a_f and b_f coefficients for aggregates given by Eq. (20). As shown in Fig. 20b, the new coefficients lead to reasonable estimates of V_t. However, despite considerable effort, we have been unable to explain the differences between Kajikawa's (1982) measurements of V_t and V_t from the calculations above 50 cm s^{-1}.

We next examine how accurately V_t can be estimated when m is unknown but can be estimated from A_r and D. These A_r values are then used to calculate m and V_t for the Kajikawa (1982) and MN65 aggregates. In general, the calculated and measured values for V_t (Fig. 20C) were in reasonable agreement; differences primarily resulted from the scatter in ρ_e for aggregates.

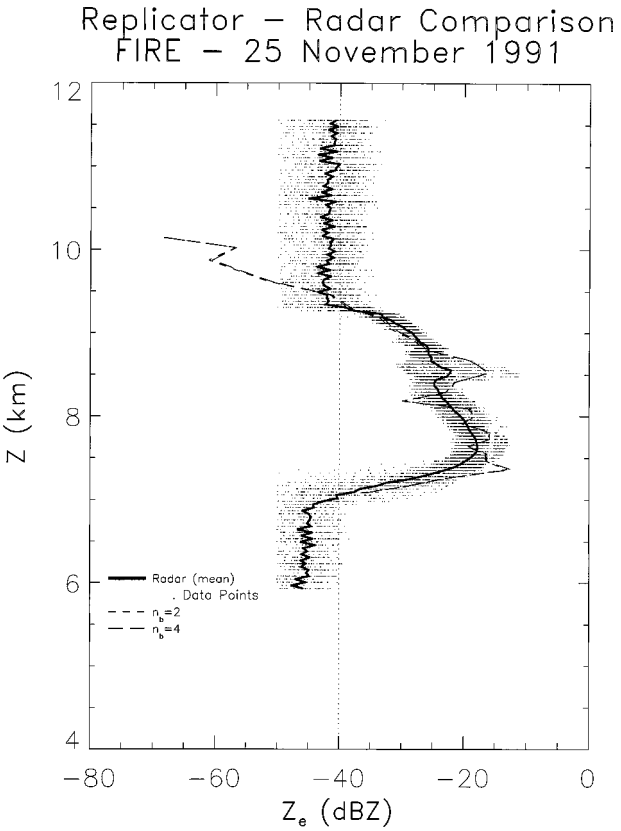

FIG. 18. Equivalent radar reflectivity (in dBZ_e) measured from NOAA K-band radar and calculated from balloon-borne ice crystal size distribution and habit data on 25 Nov 1991 near Coffeyville, Kansas (329 m MSL). Dots represent radar data points, for the period 1345–1400 UTC. Calculated dBZ_e for n_b values of 2 and 4, based on replicator size distributions, are plotted. The dotted vertical line shows approximate minimum detectable dBZ_e. Radar data courtesy Brad Orr (NOAA WPL).

We offer the following simplified means of deriving the V_t for aggregates, information that has not been adequately available in the literature. For levels other than at the surface, Eq. (19) shows that V_t is proportional to the ratio m/A, suggesting that a V_t versus D relationship can be derived if this ratio is known as a function of D. This ratio, plotted for several different types of aggregates in Fig. 21, has never been reported for aggregates based on the individual particle data. The m/A ratios were relatively independent of size for the aggregates and side-plane aggregates examined in MN65 and Kajikawa (1982), whereas a size dependence was noted for rosette aggregates.

In Fig. 21, curves of m/A versus D were derived for aggregates with several different types of component crystals from

$$\frac{m}{A} = \frac{2}{3} kDA_r^{n-1}. \tag{25}$$

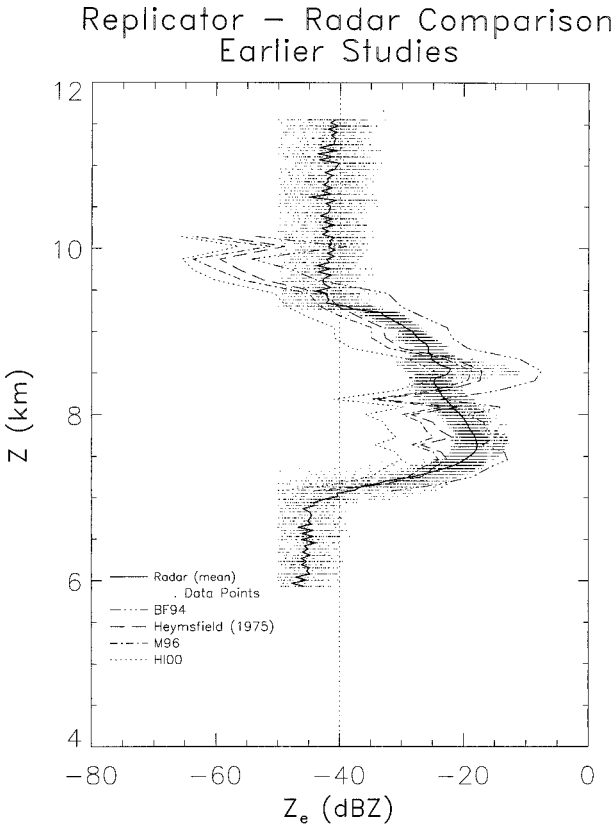

FIG. 19. Same as Fig. 18 except that calculated dBZ$_e$ are based on M96, HI00, and BF94.

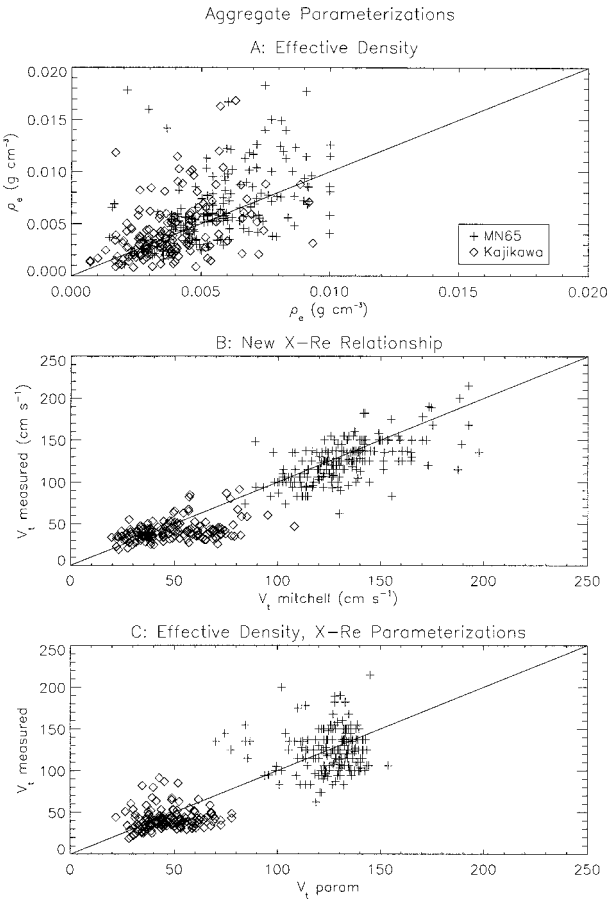

FIG. 20. The ρ_e and V_t calculated for aggregates using the A_r and D from the MN65 and Kajikawa (1982) datasets compared with the observed values. (a) Measured ρ_e vs ρ_e calculated from A_r. (b) Measured V_t vs V_t calculated from measured m, A, and D. (c) Same as (b) except that ρ_e was calculated from the two-parameter approach.

It is reasonable to use a mean value for A_r (0.68) in Eq. (25) for aggregates of planar crystals observed in the MN65 study as there was little dependence of A_r on D. Inserting the appropriate k and n yields the relationship $m/A = 0.0056D$, which applies to well developed aggregates of planar crystals. This curve fits the data points in Fig. 21a reasonably well. Likewise, using a mean A_r (0.39) for the aggregates observed in the Kajikawa (1982) study yields the relationship $m/A = 0.0063D$ for aggregates of from 2 to 6 planar crystals. This curve also fits the data points in Fig. 21a reasonably well. Similarly, taking a mean A_r value (0.46) for aggregates of side planes yields the relationship $m/A = 0.0792D$; this curve also provided a reasonable fit to the data in Fig. 21b. Finally, aggregates of rosettes did show a weak dependence of A_r on D, hence it was necessary to fit a curve to the A_r versus D values. Inserting this relationship into Eq. (25) with the appropriate k and n from Table 1 resulted in the relationship, $m/A = 0.0228D^{0.58}$, which fits the data quite well.

Combining Eq. (19) with these m/A values and the appropriate a_f and b_f coefficients from Eqs. (18) and (20), leads to the relationship

$$V_t = aD^b, \tag{26}$$

where at a temperature and pressure of −10°C and 500 hPa, $a = 160$ and $b = 0.91$ for early (Kajikawa 1982) aggregates of planar crystals in the size range $0.1 < D$ 0.6 cm and $a = 136$ and $b = 0.40$ for well-developed (MN65) aggregates of planar crystals in the size range $0.6 < D$ 3.6 cm. At a temperature and pressure of −40°C and 300 hPa appropriate for aggregates of cirrus-type particles, $a = 958$ and $b = 0.91$ for side-plane aggregates for sizes $0.05 < D$ 0.2 cm and $a = 536$ and $b = 0.68$ for rosette aggregates for sizes $0.05 < D$ 0.2 cm. The a and b coefficients for different pressure and temperature levels can be readily found through use of Eqs. (18)–(20).

5. Conclusions

Over the past 30 years, habit-dependent relationships between particle mass or terminal velocity (which depends on mass) and dimension were developed to provide a means of prescribing these properties for observational, modeling, and remote-sensing applications. Our study uses a combination of theory, numerical mod-

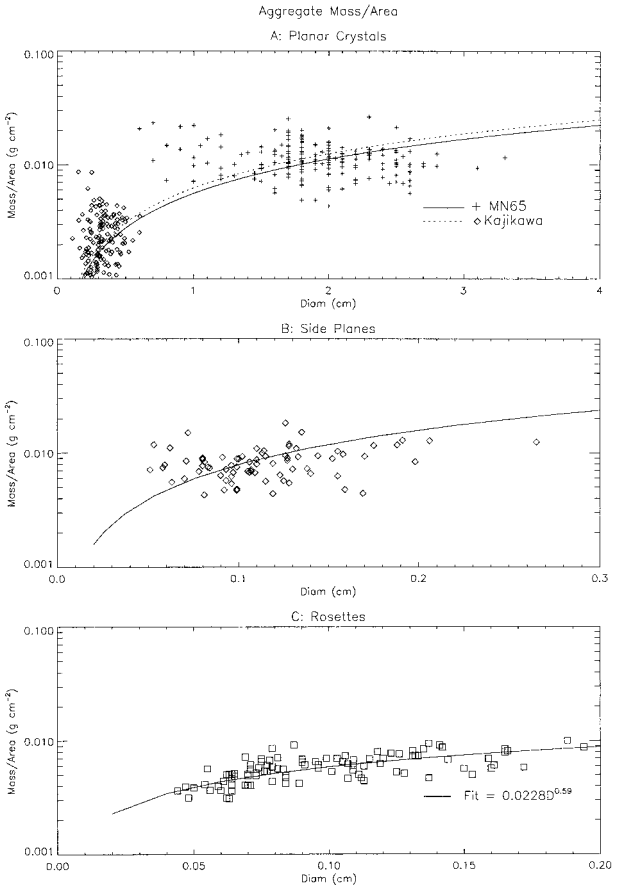

FIG. 21. Ratio of mass to area as a function of D for aggregates of indicated type. Solid lines show relationships derived for each aggregate type.

eling, and observational approaches to improve upon the reliability and generality of the one-parameter (D) method. We based our approach on the idea that A and D together, rather than D alone, were more reliable estimators of m and V_t. This two-parameter technique—when used in conjunction with particle size distribution measurements from three ice clouds sampled by aircraft and a fourth cloud sampled by our balloon-borne ice crystal replicator—produced better estimates of IWC and dBZ_e values than using D alone. The new approach was better able to capture the changes in the ice particle properties in the vertical and horizontal. The conversion of previous mass–dimensional relationships to this new technique through the use of appropriate area to dimension relationships reported in the literature resulted in improved estimates of IWC.

The two-parameter approach relied on the development of habit-dependent relationships between A_r and ρ_e of the forms $\rho_e = kA_r^n$ and $m = (\pi/6)\rho_e D^3$. This ρ_e relationship worked best for single particles. The addition of D into this relationship, $\rho_e = kA_r^n D^\alpha$, was shown to further improve the estimates of ρ_e for aggregates. Efforts should be made to relate ρ_e to A_r for more complicated crystal shapes (side planes, rimed particles) to better quantify the n and k parameters.

Using the results from the two-parameter approach for two cases of cirrus clouds comprising mainly bullet rosette crystals, it was possible to derive an explicit ρ_e and m versus D relationship for rosettes. Further study is warranted, as these relationships may vary from cloud to cloud and in the vertical for a given cloud; the relationships also depend on habit. When coupled with particle size distributions, they offer the promise of providing more reliable estimates of mean and mass-weighted fall velocities, effective radii, and radar reflectivities than have been possible in the past.

It is also recommended that more measurements of the physical properties of aggregates be acquired, for three reasons. First, more measurements would further constrain the relationships between ρ_e, A_r, and D, using consistent rather than disparate datasets. Second, the X versus Re relationship, developed in our study for aggregates in the range $0.6 < D < 3$ cm, was only an approximation because of our limited sample size; what is needed is V_t, m, and A for aggregates in this size range. Third, although we developed V_t versus D relationships for aggregates with several types of component particles, based on the ratio of m/A, more information, particularly on m and A is needed to refine the V_t versus D relationships.

Acknowledgments. The authors wish to thank T. Nakamura, T. Takahashi, N. Knight, and K. Hilburn for the use of original data for this analysis. Help from W. Hall, who developed new 2D probe processing software; J. Oppenheimer and A. Lau, who synthesized CPI images; and B. Armstrong, who edited the manuscript is greatly appreciated. Discussions with D. Mitchell, S. Matrosov, and P. Field were helpful. David Mitchell carefully reviewed this manuscript. This research was supported by funding from NASA EOS (Contract S-97894-F) and the NASA TRMM Project Office (Grant NAG5-7743).

APPENDIX A

List of Symbols

Symbol	Description
A	Particle cross-sectional area; e.g., the particle's area projected onto a horizontal plane
A_r	Area of an ice particle projected onto a horizontal surface divided by the area of a circumscribed circle
A_{rC}, A_{rB}, A_{rP}	Area ratios of simplified columns, bullet rosettes, planar crystals
A_v	Cross-sectional area of an aggregate as viewed from the side
a	Coefficient in terminal velocity–diameter relationship

a_f	Coefficient in Reynolds number–Best number relationship
b	Exponent in terminal velocity–diameter relationship
b_f	Exponent in Reynolds number–Best number relationship
D	Maximum particle dimension; the dimension of a circumscribed sphere for columns and planar crystals, the diameter of the projected image of bullet rosettes, side planes, and aggregates
D_m	Melted equivalent diameter of an ice particle, in mm
d	Dimension across basal face of hexagonal planar crystal
dBZ_e	Equivalent radar reflectivity factor
g	Gravitational acceleration constant
IWC, ΔIWC	Ice water content, difference between calculated and measured (CVI) IWC
k	Coefficient in effective density–area ratio relationship
l	Length of column, bullet
m	Ice particle mass
N	Concentration of particles of diameter D
n	Exponent in effective density–area ratio relationship
n_b	Number of bullets in rosette
Re	Reynolds number
t	Planar crystal thickness
V_t	Ice particle terminal velocity
v_b	Volume enclosing a bullet
v_b	Hollow volume of bullet
v_r	Ratio of particle volume to the volume of a circumscribed sphere. For rosettes and aggregates, the diameter of the circumscribed sphere is taken to be the projected dimension
w	Column width
x, y	Coefficient, exponent in power-law type aspect ratio-area ratio relationship
X	Best number
T	Temperature (°C)
Z_e	Equivalent radar reflectivity factor
α_C, α_B, α_P	Aspect ratios for columns (width/length), bullet rosettes (width/length), planar crystals (thickness/length)
γ, κ	Coefficient, exponent in area–diameter equation
ν	Kinematic viscosity
ρ_a	Air density
ρ_b	Bulk density; crystal mass divided by the volume of the exterior surface of a hexagonal column or bullet
ρ_e	Ice particle mass divided by the volume of a circumscribed sphere
$\rho_e C$, $\rho_e B$, $\rho_e P$	Effective density for simplified columns, bullet rosettes, planar crystals

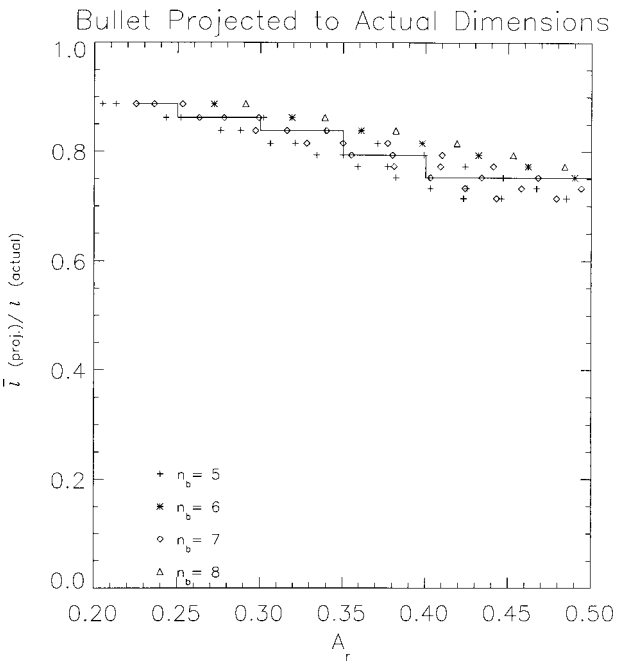

FIG. B1. Ratio of mean projected length to actual length of bullets in rosettes with n_b from 5 to 8, as a function of A_r.

ρ_w	Density of liquid water
σ, β	Coefficient, exponent in mass vs diameter equation
χ, δ	Coefficient, exponent in density vs diameter equation

APPENDIX B

Rosette Volume Calculated from Images

The ρ_e values of rosettes were estimated from images from the CPI probe. However, these were underestimates because the measured dimensions of the bullets were projections and hence were smaller than the true dimensions. The projected w of a bullet in a rosette probably had nearly the same value as the actual w, but the projected l was shorter than the actual l. The error in a bullet's volume was, therefore, proportional to the error in l to a first approximation.

The analytic model was used to estimate this error. The ratio of the mean projected l of the bullets in rosettes to the actual l was calculated for the eight-rosette configurations associated with n_b from five to eight. The α_B ranged from 0.2 to 0.6. The calculations showed that the ratio decreased from a mean of 0.88 (a difference of 12%) at $0.2 < A_r < 0.25$ to 0.74 (difference of 26%) for $0.45\ A_r < 0.50$ (Fig. B1).

REFERENCES

Auer, A. H., Jr., and D. L. Veal, 1970: The dimension of ice crystals in natural clouds. *J. Atmos. Sci.*, **27,** 919–926.

Barthazy, E., W. Henrich, and A. Waldvogel, 1998: Size distribution of hydrometeors through the melting layer. *Atmos. Res.*, **47,** 193–208.

Brown, P. R. A., and P. N. Francis, 1995: Improved measurements of the ice water content in cirrus using a total-water probe. *J. Atmos. Oceanic Technol.*, **12,** 410–414.

Detwiler, A. G., N. C. Knight, and A. J. Heymsfield, 1993: Magnitude of error factors in estimates of snow-particle masses from images. *J. Appl. Meteor.*, **32,** 804–809.

Heymsfield, A. J., 1972: Ice crystal terminal velocities. *J. Atmos. Sci.*, **29,** 1348–1357.

——, 1975: Cirrus uncinus generating cells and the evolution of cirriform clouds. Part I: Aircraft observations of the growth of the ice phase. *J. Atmos. Sci.*, **32,** 799–808.

——, and J. L. Parrish, 1978: A computational technique for increasing the effective sampling volume of the PMS 2–D particle size spectrometer. *J. Appl. Meteor.*, **17,** 1566–1572.

——, and M. Kajikawa, 1987: An improved approach to calculating terminal velocities of plate-like crystals and graupel. *J. Atmos. Sci.*, **44,** 1088–1099.

——, and J. Iaquinta, 2000: Cirrus crystal terminal velocities. *J. Atmos. Sci.*, **57,** 916–938.

Iaquinta, J., H. Isaka, and P. Personne, 1995: Scattering phase functions of bullet rosette ice crystals. *J. Atmos. Sci.*, **52,** 1401–1413.

Kajikawa, M., 1977: Observations of fall attitude of conelike graupel particles. *Mem. Fac. Edu., Akita Univ.*, **27,** 78–85.

——, 1982: Observations of the falling motion of early snowflakes. Part I: Relationship between the free-fall pattern and the number and shape of component snow crystals. *J. Meteor. Soc. Japan*, **60,** 797–803.

——, and A. J. Heymsfield, 1989: Aggregation of ice crystals in cirrus. *J. Atmos. Sci.*, **46,** 3108–3121.

Klinov, P. R., 1960. *Atmospheric Water at Low Temperatures.* USSR Academy of Sciences, 169 pp. [Available from A. Heymsfield, 3450 Mitchell Lane, Boulder, CO, 80301.]

Kobayashi, T., Y. Furukawa, K. T. Takahashi, and H. Uyeda, 1976: Cubic structure models at the junctions in polycrystalline snow crystals. *J. Cryst. Growth*, **35,** 262–267.

List, R., and R. S. Schemenauer, 1971: Free-fall behavior of planar snow crystals, conical graupel, and small hail. *J. Atmos. Sci.*, **28,** 110–115.

Locatelli, J. D., and P. V. Hobbs, 1974: Fall speeds and masses of solid precipitation particles. *J. Geophys. Res.*, **79,** 2185–2197.

Magono, C., and T. Nakamura, 1965: Aerodynamic studies of falling snowflakes. *J. Meteor. Soc. Japan*, **43,** 139–147.

——, and C. W. Lee, 1966: Meteorological classification of natural snow crystals. *J. Fac. Sci. Hokkaido Univ. Ser. 7*, **2,** 321–335.

Matrosov, S. Y., and A. J. Heymsfield, 2000: The use of Doppler radar measurements to derive ice cloud particle fall velocity relations for climate models. *J. Geophys. Res.*, **105** (D7), 22 427–22 436.

Miloshevich, L. M., and A. J. Heymsfield, 1997: A balloon-borne continuous cloud particle replicator for measuring vertical profiles of cloud microphysical properties: Instrument design, performance, and collection efficiency analysis. *J. Atmos. Oceanic Technol.*, **14,** 753–768.

Mitchell, D. L., 1996: Use of mass- and area-dimensional power laws for determining precipitation particle terminal velocities. *J. Atmos. Sci.*, **53,** 1710–1723.

——, A. Macke, and Y. Liu, 1996: Modeling cirrus clouds. Part II: Treatment of radiative properties. *J. Atmos. Sci.*, **53,** 267–2988.

Orr, B. W., and R. A. Kropfli, 1999: A method for estimating particle fall velocities from vertically pointing Doppler radar. *J. Atmos. Oceanic Technol.*, **16,** 29–37.

Pruppacher, H. R., and J. D. Klett, 1978: *Microphysics of Clouds and Precipitation.* Reidel, 714 pp.

Sasyo, Y., and T. Matsuo, 1980: On the statistical investigation of fall velocity of snowflakes. *Pap. Meteor. Geophys.*, **31,** 61–79.

Takahashi, T., T. Endoh, G. Wakahama, and N. Fukuta, 1991: Vapor diffusional growth of free-falling snow crystals between −3 and −23°C. *J. Meteor. Soc. Japan*, **69,** 15–3.

Twohy, C. H., A. J. Schanot, and W. A. Cooper, 1997: Measurement of condensated water content in liquid and ice clouds using an airborne counterflow virtual impactor. *J. Atmos. Oceanic Technol.*, **14,** 197–202.